Interatomic potential parameterization using particle swarm optimization: Case study of glassy silica

Rasmus Christensen[1], Søren S. Sørensen[1], Han Liu[2], Kevin Li[2], Mathieu Bauchy[2,*], Morten M. Smedskjaer[1,*]

[1] *Department of Chemistry and Bioscience, Aalborg University, Aalborg, Denmark*

[2] *Department of Civil and Environmental Engineering, University of California, Los Angeles, USA*

[*] Corresponding authors. E-mail: bauchy@ucla.edu (M.B.), mos@bio.aau.dk (M.M.S.)

Abstract

Classical molecular dynamics simulations of glassy materials rely on the availability of accurate, yet computationally efficient interatomic force fields. The parameterization of new potentials remains challenging due to the non-convex nature of the accompanying optimization problem, which renders the traditional optimization methods inefficient or subject to bias. In this work, we present a new parameterization method based on particle swarm optimization (PSO), which is a stochastic population-based optimization method. Using glassy silica as a case study, we introduce two interatomic potentials using PSO, which are parameterized so as to match structural features obtained from *ab initio* simulations and experimental neutron diffraction data. We find that the PSO algorithm is highly efficient at searching for and identifying viable potential parameters that reproduce the structural features used as target in the parameterization. The presented approach is very general and can be easily applied to other interatomic potential parameterization schemes.

I. Introduction

The design of new oxide glass materials with tailored properties requires an accurate understanding of their composition-structure-property relationships. The missing link in establishing such relationships is typically the glass structure, which remains challenging to characterize and predict, as glasses exhibit a complex structure with features on various length scales. This includes coordination numbers, bond angle distributions, ring size distributions, pair distribution functions, etc. and is a result of the non-equilibrium, non-crystalline nature of the glassy state.[1,2] Classical molecular dynamics (MD) simulations can serve as a computationally efficient tool to understand structure-property relations in multicomponent oxide glasses and to validate theoretical predictions as well as to provide insights into experimental observations by providing the exact location of all atoms, which remain extremely challenging to obtain with conventional experimental techniques. In addition, classical MD simulations can be used to predict, e.g., mechanical and dynamical properties from the simulated structure, and hereby aid in the design of new optimized structures with improved properties.[3]

The accuracy of classical MD simulations mostly depends on that of the underlying interatomic potential. Besides the inherently high cooling rate and small system size compared to experiments, the availability of realistic potentials is often the main bottleneck limiting the use of classical MD simulations for a range of glass families[4]. Therefore, parameterization of new and improved force fields is an important task within glass science. The parameterization of a new force field usually involves three main steps: (i) selection of an appropriate analytical form of the force field, (ii) selection of one or more features of a reference system that the force field should be parameterized to replicate (i.e., the optimization cost function), and (iii) optimization of the force field parameter values to replicate the selected features (i.e., minimize the cost function). The parameterization of a force field is therefore typically an optimization problem, wherein a given cost function needs to be minimized. Here, the cost function describes the difference in a feature of the simulated system and

that of a reference system. The latter can be experimental data or data from another more accurate simulation technique such as *ab initio* molecular dynamics (AIMD).[4]

The accuracy of a parameterized potential greatly depends on the two first steps and these steps indeed receive the most attention in the literature[4]. Nonetheless, the optimization algorithm in step (iii) is also important, but has not received much attention. Conventional gradient-based optimization techniques like conjugate gradient, steepest descent, and Levenberg Marquardt are commonly used for optimization of the cost function in potential parameterizations.[5,6] However, these algorithms can be inefficient at exploring rough cost landscapes, as they only progress towards the first local minimum found and will thus not explore the cost landscape, unless the optimization process is reinitiated by the user.[5,7] As parameterization of a new potential involves a large number of parameters, cost landscapes can be highly non-convex and exhibit a large number of local minima, thereby rendering traditional optimization methods inefficient or subject to bias. It is thus interesting to investigate alternative and possibly more efficient optimization techniques for optimization of the cost function, as it could enable faster iteration on the design of cost functions and hence faster exploration and development of new interatomic potentials.

A recent attempt to use an alternative optimization method for potential parameterization is that of Liu *et al.*[7], who used Bayesian optimization, a type of machine learning, to successfully parameterize an interatomic potential for glassy silica. This was done by comparing the partial pair distribution functions (PDFs) of a silica melt at 3600 K obtained from classical MD and AIMD simulations, similar to the work of Carré *et al.*[6]. Another interesting optimization method for potential parameterization is particle swarm optimization (PSO). PSO is a stochastic population-based optimization method with a straightforward mechanism that, unlike, for instance, gradient descent, does not require any gradient information, making it easy to implement for most optimization problems. As the PSO method only contains few algorithm parameters, which are widely discussed in literature[8], it is suitable as a non-biased optimization method where the role of personal intuition

during optimization is reduced. PSO has previously been applied for parametrization of potentials for crystalline metals and alloys[9,10], but not yet on glasses.

In this work, we present a new methodology for efficient parameterization of interatomic pair potentials for glasses based on PSO. Here glassy silica, an archetypal ionocovalent composition, is chosen as the model system, while the well-known two-body Buckingham potential is chosen as the analytical formulation of the force field, as it has previously been shown to accurately describe glassy silica in other potentials.[6,11,12] Specifically, we parametrize two force fields. The first, referred to as PSO-1, is parameterized with respect to AIMD structural data of liquid silica at 3600 K, analogous to what has been done recently for the machine learning force field[7]. The PSO approach is suitable in this case, since the cost landscape resulting from this parameterization method is known to be rough and difficult for gradient based methods to optimize, while enabling easy comparison to the recent machine learning optimization approach.[7] The second, referred to as PSO-2, is parameterized from comparison to experimental neutron scattering data of glassy silica[13]. To this end, we note the inherent difficulties in potential parameterization from experimental data of the glassy state due to the difference in cooling rate between simulations and experiments. However, the goal of these two parameterization methods is not to produce a state-of-the-art potential for silica glass or offer new physical insights into the behavior of glassy silica, but rather to highlight the efficiency of the PSO algorithm and to explore the nature of the resulting potentials. From these optimizations, we show that the PSO-based method allows us to quickly and robustly identify force field parameters, which accurately replicate the selected features of the AIMD and experimental data.

II. Methods

A. Simulations of silica

All molecular dynamics simulations were conducted using the Large-scale Atomic/Molecular Massively Parallel Simulator (LAMMPS) program developed by Sandia National Laboratories.[14] We

used the Buckingham functional form for the interatomic potentials parameterized in this work[6,11], including a short-range r^{24} repulsive term,

$$U(r_{ij}) = \frac{q_i q_j}{4\pi r_{ij}\epsilon_0} + A_{ij}\exp\left(-\frac{r_{ij}}{\rho_{ij}}\right) - \frac{C_{ij}}{r_{ij}^6} + \frac{D_{ij}}{r_{ij}^{24}}, \quad (1)$$

where $r_{ij}$is the distance between atom i and j, q_i and q_j are the partial charges of atom i and j (ensuring $q_O = -\frac{q_{Si}}{2}$), respectively, and ϵ_0 is the permittivity of vacuum, while A_{ij}, ρ_{ij}, C_{ij} and D_{ij} are the potential parameters describing the short range interactions. The last term $\frac{D_{ij}}{r_{ij}^{24}}$ was added to prevent the "Buckingham catastrophe". A cutoff of 8 Å was used for short-range interactions, while the long-range Coulombic interactions were evaluated using the damped shifted force model[15] with a cutoff of 8 Å and damping parameter of 0.25, as also used elsewhere.[7] We note how this approximate Coulombic interaction may result in a slight decrease in accuracy, yet significantly lowers the computational cost (up to ten times faster compared to using Ewald summation on the used hardware), thus making both parameterization and resulting MD simulations significantly faster. Such approximation has previously been used successfully to produce interatomic pair potentials of oxide glasses[5,7], and has been shown to only have a minor effect on the accuracy when used in simulations with other potentials.[16,17] Interactions between silicon atoms were evaluated as purely Coulombic, as done in several previous silica potentials[7,11,12,18], due to the short range interactions of this atom pair only having a small effect on the accuracy of the final potential.[19] The values of D_{ij} were fixed in all the simulations based on values from Carré *et al.*,[6] (D_{ij} = 113, 29, and 3,423,200 eV·Å^{24} for O–O, Si–O, and Si–Si interactions, respectively). This was done since this term only prevents unrealistic overlap of atoms.

All simulations were conducted with a timestep of 1 fs and using an initial configuration of 1000 SiO_2 units (3000 atoms) in a periodic cubic simulation box with a side length of 35.661 Å, corresponding to a density of 2.2 g·cm^{-3}. Simulations conducted for recording structural data of silica in the liquid phase were performed by first relaxing the box for 10 ps at 3600 K in the *NVT* ensemble,

where after the liquid silica structure was recorded as a statistical average over 10 ps (sampling every timestep).

Silica glasses were simulated using the following melt-quench procedure, with all procedures conducted in the *NPT* ensemble. The system was first melted at 3600 K at for 100 ps to erase any history of the initial state. The system was then quenched to 300 K with a cooling rate of 1 $K \cdot ps^{-1}$, producing a disordered glass structure. A hydrostatic pressure of 0.1 GPa was applied during melting for the parameterization of PSO-2 to avoid the system entering the gas phase at very high temperatures, while zero pressure was applied for all other potentials. The pressure of 0.1 GPa was ramped down to 10^{-4} GPa during the quenching process. The resulting glasses were relaxed for 100 ps at 300 K and 10^{-4} GPa pressure, before the simulated glass structures were recorded for another 100 ps for statistical averaging (sampling every 1 ps).

For comparison, we also conducted simulations with several alternative potentials from literature, namely the BKS potential by Van Beest *et al.*[11], the CHIK potential by Carré *et al.*[6], the SHIK potential by Sundararaman *et al.*[5], and the machine learning (ML) potential by Liu *et al.*[7]. Simulations with these alternative potentials were conducted according to the requirements described in those previous studies[5–7,11], but with the simulation procedure for obtaining liquid and glassy silica as described above. However, a slight modifications was made for the BKS potential, as the cutoff for the short range interactions was set to 5.5 Å and the long range interactions were evaluated with the PPPM algorithm using an accuracy of 10^{-5}, as reported elsewhere[17].

B. Optimization cost functions

Next, we consider the optimization cost function used in this work. For the parametrization of potentials based on the simulated structure of liquid silica, the difference between partial PDFs (described in Section II.C) from classical MD and AIMD was used. Specifically, we used partial

PDFs from Car-Parrinello molecular dynamics of liquid silica at 3600 K.[7] The difference between the partial PDFs obtained from classical MD and AIMD was defined as an $R_\chi^{g(r)}$ error[6,7],

$$R_\chi^{g(r)} = 100\% \cdot \sqrt{\frac{\chi_{\mathrm{SiO}}^2 + \chi_{\mathrm{OO}}^2 + \chi_{\mathrm{SiSi}}^2}{3}}, \quad (2)$$

where χ_{ij}^2 capture the level of agreement between each partial PDF obtained by MD and its counterpart obtained by AIMD as described by,

$$\chi_{ij}^2 = \frac{\sum_r \left[g_{ij}^{\mathrm{AIMD}}(r) - g_{ij}^{\mathrm{MD}}(r)\right]^2}{\sum_r \left[g_{ij}^{\mathrm{AIMD}}(r)\right]^2}, \quad (3)$$

where $g_{ij}^{\mathrm{AIMD}}(r)$ and $g_{ij}^{\mathrm{MD}}(r)$ are the partial PDFs for the pair of atoms i and j from AIMD and classical MD simulations, respectively. As $R_\chi^{g(r)}$ captures the total level of agreement between partial PDFs from classical MD and AIMD, it was used as a cost function for parametrizing potentials with PSO.

Similarly, for parameterizing potentials based on the simulated glass structure, the level of agreement between the differential correlation function $D(r)$ (described in Section II.C) of silica glasses based on neutron scattering experiments[13] and from the present simulations was compared through an $R_\chi^{D(r)}$ error as,

$$R_\chi^{D(r)} = 100\% \cdot \sqrt{\frac{\sum_r [D(r)^{\mathrm{exp}} - D(r)^{\mathrm{sim}})]^2}{\sum_r [D(r)^{\mathrm{exp}}]^2}}. \quad (4)$$

We note that the $R_\chi^{D(r)}$ function is not directly comparable to χ_{ij}^2. That is, $R_\chi^{D(r)}$ puts a more significant weight on medium-range order structure than χ_{ij}^2. This is because $D(r) \to 0$ for $r \to \infty$, in contrast to the continuously increasing denominator in Eq. (3) as $g_{ij}(r) \to 1$ for $r \to \infty$ because of the lack of long-range order in the glassy structures.

C. Pair distributions functions and structure factors

To compare the structure of the simulated silica liquids and glasses with experimental data from neutron diffraction, or structure data from *ab initio* simulations, we computed the partial PDFs of the system as,

$$g_{ij}(r) = \frac{n_{ij}(r)}{4\pi r^2 \mathrm{d}r \rho_0}, \tag{5}$$

where $n_{ij}(r)$ is the number of particles of type *j* between the distances *r* and *r* + *dr* from a particle of type *i*, while ρ_0 is the average atomic number density[20]. From the partial PDFs, the total PDF can be calculated as,

$$G(r) = \left(\sum_{i=1}^{n} c_i \bar{b_i}\right)^{-2} \sum_{i,j=1}^{n} c_i c_j b_i b_j g_{ij}(r), \tag{6}$$

where c_i is the fraction of atoms *i* and b_i is the neutron scattering length of atom type *i.* [20] For silica, the neutron scattering lengths are 4.1491 and 5.803 for silicon and oxygen, respectively. [21]

To enable comparison between simulated and experimental PDFs, broadening of the simulated PDF is needed due to the broadening of the experimental PDF as caused by the finite scattering vector cutoff of the Fourier transform of the structure factor. To do so, the PDF was convoluted by a normalized Gaussian distribution with a full width at half-maximum (FWHM) given by FWHM = 5.437/$Q_{\max}$, where $Q_{\max}$ is the maximum wave vector used in the diffraction experiment.[22,23]

From the total pair distribution function, the differential correlation function $D(r)$, sometimes also denoted as the reduced pair distribution function, was calculated as [24],

$$D(r) = -4\pi\rho_0 r + 4\pi\rho r G(r). \tag{7}$$

For further comparison of potentials, the total neutron structure factor ($S(Q)$) was calculated. To this end, the Faber-Ziman partial structure factors $S_{ij}(Q)$ were first calculated from the partial PDFs as,

$$S_{ij}(Q) = 1 + \rho_0 \int_0^{r_{\max}} 4\pi r^2 \left[g_{ij}(r) - 1\right] \frac{\sin\,(Qr)}{Qr}\, dr, \tag{8}$$

where Q is the scattering vector and $r_{\max}$ is the maximum radius for the integration (in this case half the simulation box size because of periodic boundary conditions). The total neutron structure factor, $S(Q)$, was then calculated from the partial structure factors as,

$$S(Q) = \left(\sum_{i=1}^{n} c_i \bar{b_i}\right)^{-2} \sum_{i,j=1}^{n} c_i c_j b_i b_j S_{ij}(Q). \tag{9}$$

To enable comparison between $S(Q)$ predicted by different potentials, we introduce an $R_\chi^{S(Q)}$ error similar to Eq. (4),

$$R_\chi^{S(Q)} = 100\% \cdot \sqrt{\frac{\sum_r [S(Q)^{\exp} - S(Q)^{\mathrm{sim}})]^2}{\sum_r [S(Q)^{\exp}]^2}}, \tag{10}$$

where $S(Q)^{\exp}$ is taken from literature[13]. $S(Q)$ data from Q = 0.85 to 35 Å^{-1} was included in the calculation of $R_\chi^{S(Q)}$.

D. Calculation of vibrational density of states

The vibrational density of states (VDOS) was calculated by first determining the dynamical matrix (**D**), i.e., the matrix with elements as

$$D_{i,j}^{\alpha,\beta} = \frac{1}{\sqrt{m_i m_j}} \left(\frac{\partial^2 U}{\partial u_{i,\alpha} \partial u_{j,\beta}}\right) \tag{11}$$

through a finite displacement method. Here, m is mass of the atoms, U is the total potential energy, α and β represent the Cartesian indices, i and j are atomic indices, and u is atomic displacement. Hereafter the eigenvalues, corresponding to the frequencies of the eigenmodes, were obtained by diagonalizing the matrix by solving the matrix equation,

$$\mathbf{e} \cdot \Omega = \mathbf{D} \cdot \mathbf{e}, \tag{12}$$

where **e** is the matrix of eigenvectors and Ω is the diagonal matrix with $3N$ squared eigenvalues, ω^2, where N is the number of atoms in the system. These eigenvalues correspond to the vibrational frequencies of the eigenmodes and hence describe the VDOS of the structure.

E. Calculation of elastic properties

Besides comparison of structural features, we also calculated the elastic properties of the quenched silica glasses for the new PSO potentials and selected potentials from literature. These quenched glasses were subjected to stepwise elongations of $\varepsilon = 0.0001 = 0.01\%$ in the tensile directions *xx*, *yy*, and *zz*, as well as in the shear directions *xy*, *xz*, and *zy* under the assumption of isotropic structures. Between each elongation step, the structures were relaxed for 2 ps, before measuring the average stress in the given direction over 1 ps (sampling at every time step). Both simulation steps were conducted at 300 K in the *NVT* ensemble. We performed 60 elongations in each direction. From the resulting stress-strain curves, the elastic constants were obtained by linear regression, where C_{11} was evaluated as an average of C_{11}, C_{22}, and C_{33}, and C_{44} as an average of C_{44}, C_{55}, and C_{66}. Finally, C_{12} was calculated as $C_{12} = C_{11} - 2C_{44}$ under the assumption of isotropy. This enabled a calculation of Young's modulus (E) and Poisson's ratio (ν) as follows [25],

$$E = \frac{(C_{11} - C_{12})(C_{11} + 2C_{12})}{C_{11} + C_{12}}, \tag{13}$$

$$\nu = \frac{C_{12}}{C_{11} + C_{12}}. \tag{14}$$

F. Calculation of ring size distribution

The ring size distribution in the simulated glasses was calculated by considering the primitive rings, i.e., the shortest closed loop that includes a given Si atom and two of its nearest neighbor O atoms.

We have used the R.I.N.G.S. code[26] to determine this, up to a ring size of 12—wherein the ring size is defined in terms of the number of Si atoms the ring is comprised of.

G. Force field optimization with PSO

Particle swarm optimization (PSO) is a swarm intelligence optimization technique developed by Eberhart and Kennedy, which mimics the social behavior of animals such as bird flocking.[8] PSO offers an efficient method to identify the minimum position of a function with *n* input variables. In this approach, each unique set of parameters is represented by a point in an *n*-dimensional space, where *n* is the number of variables. Such points are denoted as particles (e.g., birds exploring a given space). These particles traverse the *n*-dimensional solution space of a given optimization problem, for several iterations seeking an optimal solution (that is, the global minimum of the target function). In PSO, all particles are initially placed randomly in the given search space within a predetermined set of boundaries, the values of which depend on the optimization problem.[27]

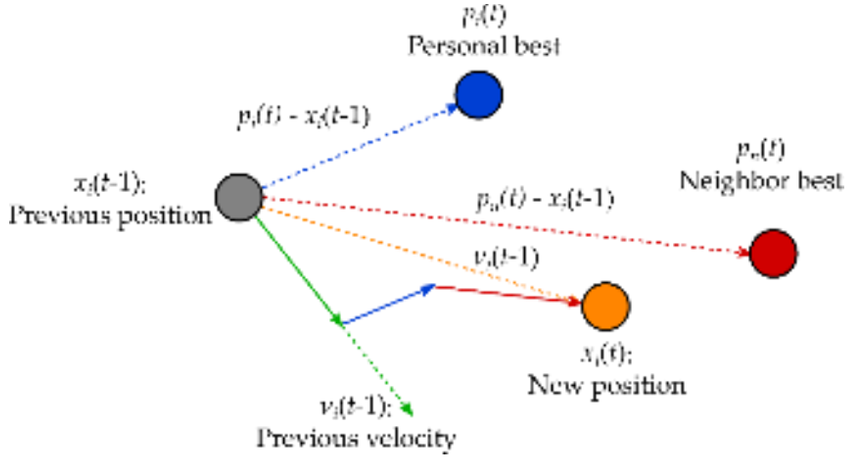

Figure 1: Movement of a particle in PSO and the velocity update. Figure is adapted from ref. [28]

The movement of a particle in two dimensions with PSO is illustrated in Figure 1. Particle positions are adjusted at each iteration from a set of stochastic velocities calculated at the current iteration. These velocities are vectors representing particle-movements in the *n*-dimensional solution space.

The velocity is updated according to three factors: (i) the personal best position (p_g), i.e., the best position (wherein the optimization function is as small as possible) visited by the particle itself so far, (ii) the best position found by the particle's neighbors (p_n, see below), i.e., the best position visited by a neighboring particle so far, and (iii) the inertia of the particle ($v_{ij}(t-1)$), i.e., the velocity of the particle at the previous iteration. From these factors, the velocity of particle i in dimension j at iteration t ($v_{ij}(t)$) can be calculated,

$$v_{ij}(t) = w \cdot v_{ij}(t-1) + c_1 r_{1,j}\left(p_i(t) - x_{ij}(t-1)\right) + c_2 r_{2,j}\left(p_n(t) - x_{ij}(t-1)\right), \quad (15)$$

where (c_1, c_2) are acceleration coefficients, w is an inertia weight, ($r_{1,j}$, $r_{2,j}$) are random numbers in the range [0,1], $v_{ij}(t-1)$ is the previous velocity of the particle, and $x_{ij}(t-1)$ is the previous particle position. Based on the calculation of velocity, the particle's position at iteration j (i.e., $x_{ij}(t)$) can be calculated,

$$x_{ij}(t) = x_{ij}(t-1) + v_{ij}(t). \quad (16)$$

This process is then repeated either for a certain number of iterations, or until the entire swarm has converged toward the same minimum.[8,28,29] Of course, it should be noted that the best minimum found with the PSO algorithm may not be the global minimum.

Several methods for determining the neighborhood of particles in PSO have been proposed. The original PSO algorithm uses the so-called global best model, which is based on a global neighborhood topology, where all particles are neighbors with each other (Fig. 2a).[29,30] A different approach is the so-called local best model, which is based on a local neighborhood ring topology (Fig. 2b).[29,30] In the latter case, particles are only neighbors to their immediate neighbors determined according to the particles index, i.e., the second particle is neighbor with the first and third particles.

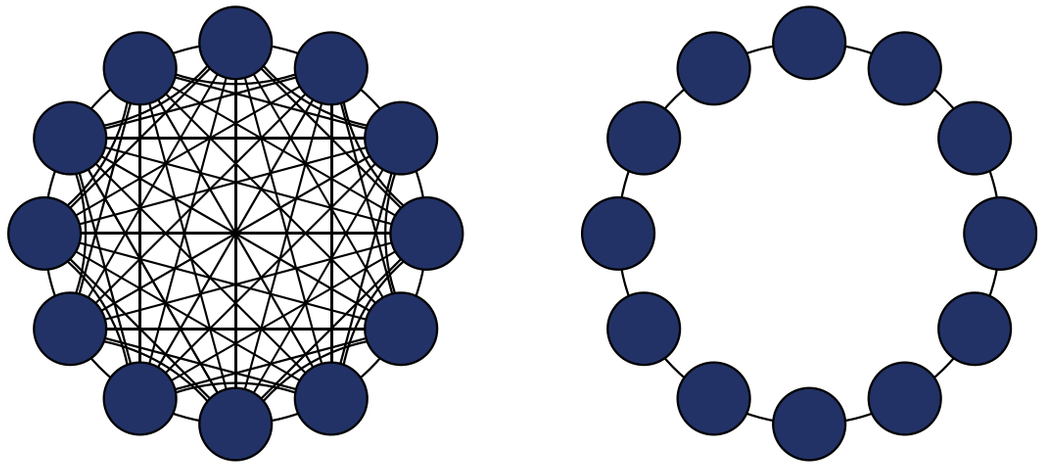

(a) global best topology (b) local best topology

Figure 2: Different neighborhood topologies for PSO (a) global best topology and (b) local best topology. Figure is adapted from ref.[29]

In general, the global best topology has been found to converge very quickly toward a minimum, but also tends to fail to find the best region of the search space.[29,31] We have found the same in preliminary calculations for this study. The local best model is comparatively slower, but able to explore more of the parameter landscape and has thus been shown to give improved optima for rough multimodal cost functions.[29,31] This improved performance is achieved, since the ring topology slows down the flow of information, enabling particles to collaboratively search several regions of the search space simultaneously.[29,31] Consequently, we used the local best neighborhood topology in this study.

We chose values of $c_1 = c_2 = 1.49618$ and $w = 0.7298$ for the algorithm based on standard values from literature to ensure convergence of the swarm[8,32], while 21 particles were used for the optimizations. For the first iteration, all particle positions were randomly initialized inside a set of search space boundaries and given a random velocity of 5% of the search space in each direction. Table I summarizes the search space boundaries used for random initialization of the particle positions.

Table I: Search space boundaries for the present silica potential parameterization with PSO.

	$A_{\text{O-O}}$ (eV)	$\rho_{\text{O-O}}$ (Å)	$C_{\text{O-O}}$ (eV·Å^6)	$A_{\text{Si-O}}$ (eV)	$\rho_{\text{Si-O}}$ (Å)	$C_{\text{Si-O}}$ (eV·Å^6)	q_{Si} (-)
Min value	0	0	0	0	0	0	1
Max value	2000	1	200	60000	0.5	250	3

Due to the random initial placement of particles in the search space, and the stochastic nature of the PSO algorithm, several simulations in an optimization will not be completed due to "bad dynamics", making it impossible to evaluate the cost of these particle positions. In these cases, the cost was set to an arbitrarily high cost not achievable from completed simulations. When initializing the particle swarm, we ensured that p_n can be determined for all particles from completed simulations, i.e., every particle either completed its simulation or had a neighbor that completed its simulation. This was achieved by ensuring at least one third of initial particles completed their simulation and randomizing the neighbors of particles until this requirement was achieved. If a particle has only tested particle positions, for which simulations could not be completed, we used its newest position (i.e., from the previous iteration) as its p_i value.

A velocity clamp $V_{\max,j}$ of 100% of the search space was used to limit the maximum value of the velocity in each direction. Furthermore, an absorbing wall boundary handling method[33] was used for the lower search space boundary to restrict the PSO algorithm to only consider positive values of A_{ij}, ρ_{ij}, and C_{ij}, as negative values are physically unrealistic. In this boundary handling method, when a particle was about to cross the lower boundary of the search space in a dimension, the value of the particle is instead set to the value of the lower boundary with its velocity zeroed in that dimension.

III. Results and Discussion

In this section, we will first compare the performance of the two potentials parameterized with PSO, described by the value of the cost function R_χ, with alternative silica potentials from the literature. Second, we will evaluate the ability of the new PSO potentials to describe the features of silica glass, which were not included in the cost function. This is done by comparing the predicted elastic properties, bond angle distributions, structure factors, ring size distribution, and vibrational properties of silica glasses simulated with the present PSO method as well as literature potentials and experimental data. The obtained force field parameters after the optimization of the two proposed cost functions are listed in Table II. Potential curves for the pair interactions of the PSO potentials compared to select potentials from literature can be found in Supplementary Figure S1.

Table II: MD force field parameters of the two PSO-based interatomic potentials.

Potential-ID	$A_{\text{O-O}}$ (eV)	$\rho_{\text{O-O}}$ (Å)	$C_{\text{O-O}}$ (eV·Å^6)	$A_{\text{Si-O}}$ (eV)	$\rho_{\text{Si-O}}$ (Å)	$C_{\text{Si-O}}$ (eV·Å^6)	q_{Si} (-)
PSO-1	883	0.360	50.4	28954	0.185	111.9	1.79
PSO-2	1522	0.366	17.4	44409	0.187	201	2.35

We observe that the potential parameters obtained for PSO-1 and PSO-2 are significantly different. For PSO-1, the partial charge of silicon is 1.79, close to the values obtained by the SHIK[5], CHIK[6], and ML[7] potentials, all of which are at least partially parameterized to replicate structural features of liquid silica. Meanwhile we observe a silicon charge of 2.35 for PSO-2, which is close to the value in the BKS[11] potential. Using the terminology of "hard" and "soft" potentials presented by Liu *et al.*[34], we may categorize the PSO-1 potential as a "soft" potential given its low partial silicon charge ($q_{\text{Si}} < 2$), while the PSO-2 potential can (almost) be classified as a "hard" potential due to its higher partial silicon charge ($q_{\text{Si}} \geq 2.4$). The importance of this classification will be discussed in Section III.C.

A. Performance of the PSO-1 potential

First, we compare the ability of the new PSO-1 potential to describe the partial PDFs in the SiO_2 melt at 3600 K relative to that of some reference potentials (Table III). We find that the PSO-1 potential exhibits the lowest obtained global $R_\chi^{g(r)}$ of 7.5%, which is an improvement relative to the alternative potentials. As the PSO-1 has specifically been trained on these data, it is expected to have a low $R_\chi^{g(r)}$, but it is notable that its $R_\chi^{g(r)}$ is lower than that of the ML potential[7], which has been parameterized with the same cost function. Moreover, the SHIK[5] and CHIK[6] potentials both include parameters for the Si – Si interaction, making these potentials more complex.

Table III: Comparison of the new PSO-1 potential (optimized against *ab initio* equilibrium liquid silica structure) with selected alternative potentials from literature, namely, BKS[11], ML[7], SHIK[5], and CHIK[6]. Average standard deviation of the global $R_\chi^{g(r)}$ is 0.1%.

Potential-ID	$R_\chi^{\mathrm{SiO}}(\%)$	$R_\chi^{\mathrm{OO}}(\%)$	$R_\chi^{\mathrm{SiSi}}(\%)$	Global $R_\chi^{g(r)}(\%)$
PSO-1	7.2	3.6	10.2	7.5
BKS	21.3	12.8	15.4	17.0
ML	7.2	3.5	12.9	8.7
SHIK	7.4	3.6	10.7	7.8
CHIK	13.0	6.0	11.9	10.7

Figure 3 shows the partial PDFs Si–O, O–O, and Si–Si as calculated based on the PSO-1 potential. For comparison, partial PDFs from AIMD are shown along with the partial PDFs predicted by the ML[7] and BKS[11] potentials. The PSO-1 potential offers a very good description of the AIMD partial PDFs and generally resemble those predicted by the ML potential. The largest difference between the PSO-1 and AIMD partial PDFs come from the Si–Si partial PDF, where the average Si–

Si distance is slightly higher in the AIMD simulation. As reported in Table III for all the applied potentials, the Si–Si partial PDF has a major contribution to the global $R_\chi^{g(r)}$, with R_χ^{SiSi} above 10% in every case. This might therefore be attributed to an intrinsic limitation of the Buckingham potential form.

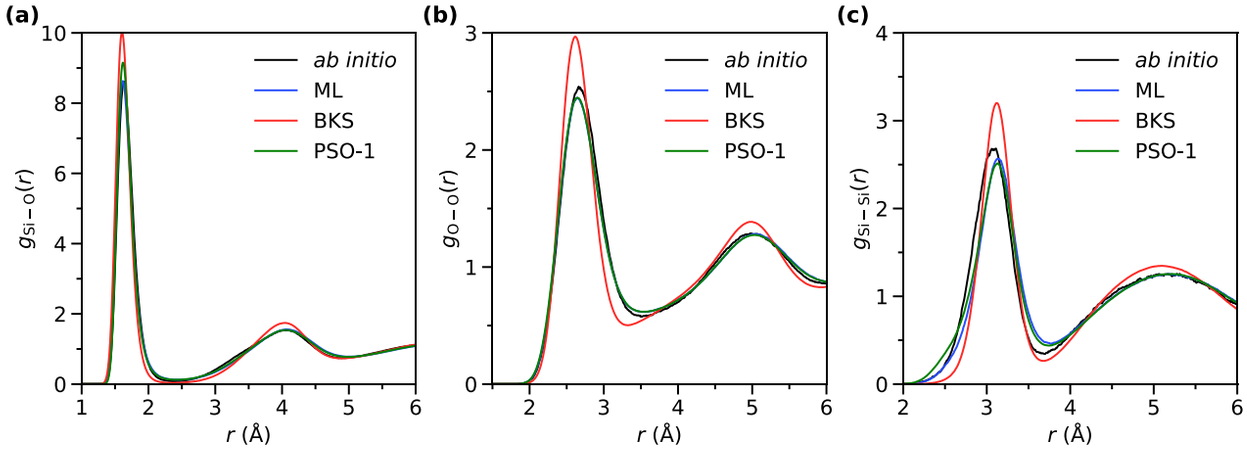

Figure 3: (a) Si–O, (b) O–O, and (c) Si–Si partial PDFs in liquid silica (at T = 3600 K) predicted by PSO-1 (green line) compared with the BKS[11] (red line) and ML[7] (blue line) potentials as well as the *ab initio* reference (black line)[7].

B. Performance of the PSO-2 potential

Next, we compare the ability of the new PSO-2 potential to describe the experimental differential correlation function ($D(r)$) of silica glass relative to that of some reference potentials. In Figure 4, we observe that the PSO-2 potential describes the experimental $D(r)$ data very well. The $R_\chi^{D(r)}$ for each potential is listed in Table IV, with the PSO-2 potential yielding a $R_\chi^{D(r)}$ value of 20.9%. We note that the R_χ functions from Eqs. (2) and (4) for calculation of $R_\chi^{g(r)}$ and $R_\chi^{D(r)}$, respectively, employ different scattering functions for comparison, thus not enabling direct comparison between the obtained values of these two R_χ. Compared to the SHIK and BKS potentials (with $R_\chi^{D(r)}$ values of 36.2% and 30.8%, respectively), this is a significant improvement. It is, however, not surprising as

the SHIK and BKS potentials were optimized against different cost functions. Nonetheless, it indicates that the PSO-2 potential generates a realistic silica glass structure, better than that offered by currently available potentials.

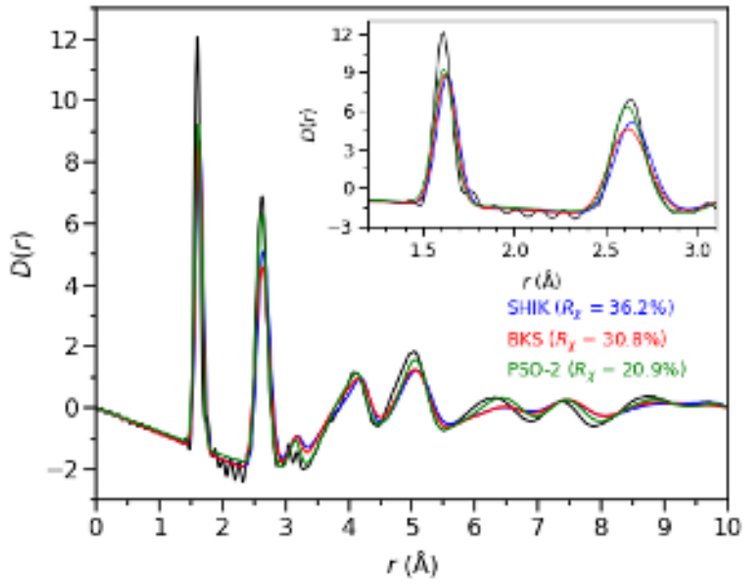

Figure 4: Differential correlation function, $D(r)$, of quenched silica glass predicted by the present PSO-2 potential compared with experimental reference data (black line)[13] as well as the $D(r)$ predicted by the SHIK[5] (blue line) and BKS[11] (red line) potentials.

Table IV: Predicted $R_\chi^{D(r)}$ error, density (ρ), Young's modulus (E), and Poisson's ratio (ν) of silica glasses structures obtained with the PSO potentials and selected potentials from the literature (BKS [11], ML[7], and SHIK[5]). Comparison with experimental data from literature[35] is also included.

Potential-ID	$R_\chi^{D(r)}$	ρ (g·cm^{-3})	E (GPa)	ν (-)
Experimental	-	2.20	72.2	0.168
PSO-1	43.3	2.12	63.1	0.248
PSO-2	20.9	2.05	154.4	0.246

SHIK	36.2	2.22	67.3	0.222
BKS	30.8	2.25	87.0	0.243
ML	43.7	2.17	63.4	0.249

C. Comparison of predicted features

To determine the ability of new PSO-based potentials to reproduce different features of silica glass, we report the MD-simulated density, Young's modulus, and Poisson's ratio of silica glasses using the PSO-1 and PSO-2 potentials (Table IV). We also include a comparison with several alternative potentials and experimental results. We observe that the PSO-2 potential overestimates the Young's modulus of silica glass by a factor of ~2. In contrast, the PSO-1 potential predicts a more realistic modulus of 63.1 GPa. The inability of the PSO potentials to accurately reproduce the mechanical properties is not surprising, considering that these potentials were not parameterized to replicate these properties.

The overestimation of Young's modulus by PSO-2 may be because this potential has been optimized against structural features of the nonequilibrium glass phase. Glasses prepared by MD simulations will typically be very disordered and feature very high fictive temperatures[36] due to the high cooling rate applied in the simulation. The force field might therefore need to be "harder" than expected to force the glass to become as ordered as an experimental glass (prepared with slower cooling rate), thus leading to an overestimation of the interatomic bond strength. As such, the good agreement between experimental and simulated structural features for PSO-2 might be a consequence of a mutual compensation of errors (e.g., overestimated bond strength compensates the high cooling rate). This compensation could affect the potential's ability to reproduce properties such as Young's modulus, which depend on the curvature of the potential minimum, as this curvature could be affected by this compensation. An alternative explanation could be that the PSO-2 potential is only parameterized to replicate the glass structure at room temperature. The shape and curvature of the

potential may only have a minor influence on this replication, as this property is mostly determined by the position of the potential well. In contrast, as the parameterization of the PSO-1 potential is conducted at 3600 K, atoms will move around their equilibrium position, thus better exploring the potential shape and with a larger influence on property used for parameterization. This, in turn, leads to an improved prediction of the curvature around the potential minimum and therefore the elastic properties of the glass. As such, while parameterizing potentials to reproduce the experimentally observed glass structure can provide a good replication of this structure, this approach will limit the ability of the potential to predict other properties which are not directly dependent on these structural details of the glass, but rather a function of the shape of the potential well (e.g., depth, curvature, or degree of asymmetry).

This is further supported by considering the calculated VDOS from PSO-2 as shown in Supplementary Figure S2b. We observe that the PSO-2 potential fails to capture the features of the VDOS from *ab initio* simulation. In contrast, the VDOS calculated using the PSO-1 potential (Supplementary Figure S2a) shows relatively good agreement with the *ab initio* MD data. Comparisons of these *ab initio* VDOS data with that calculated from the SHIK and BKS potentials are also presented in Supplementary Figure S2, with SHIK showing the best agreement, similar to the performance of the PSO-1 potential. The fact that the PSO-1 potential shows good agreement with reference VDOS data is interesting, given the difficulty of many interatomic pair potentials in correctly predicting the vibrational properties of glass systems and when considering that the PSO-1 potential was not specifically optimized against these data. The fact that PSO-2 overestimates the Si–O stretching frequency in the VDOS is consistent with the facts that the potential (i) overestimates the stiffness of the glass, (ii) presents a very sharp, deep Si–O interaction as seen in Supplementary Figure S1, and (iii) underestimates the increase in density of the glass under pressure (see Figure 8).

Furthermore, we observe a close similarity between the properties predicted by simulations using the PSO-1, SHIK, and ML[7] potentials (Table IV). Even though these potentials have an identical

potential structure, the potential parameters are significantly different. It is therefore notable that these potentials give an almost identical description of silica glass might be because these potentials can all be classified as "soft"[34] with a low silicon partial charge. This exemplifies the fact that the optimization cost function is extremely rough and exhibits many competitive minima—which further justifies the need to use a complex optimization method like PSO to explore this rough landscape.

To further compare the obtained structures, we also investigate the partial bond angle distributions (PBADs) predicted by the two new potentials (Figure 5). We note that for both PSO-1 and PSO-2, the PBADs are not included in the cost functions and such 3-body correlations are not fully described by neither the partial PDFs nor the $D(r)$. As such, the PBADs enable structural comparison with the alternative potentials for a feature, which has not been used in any of the parameterizations.

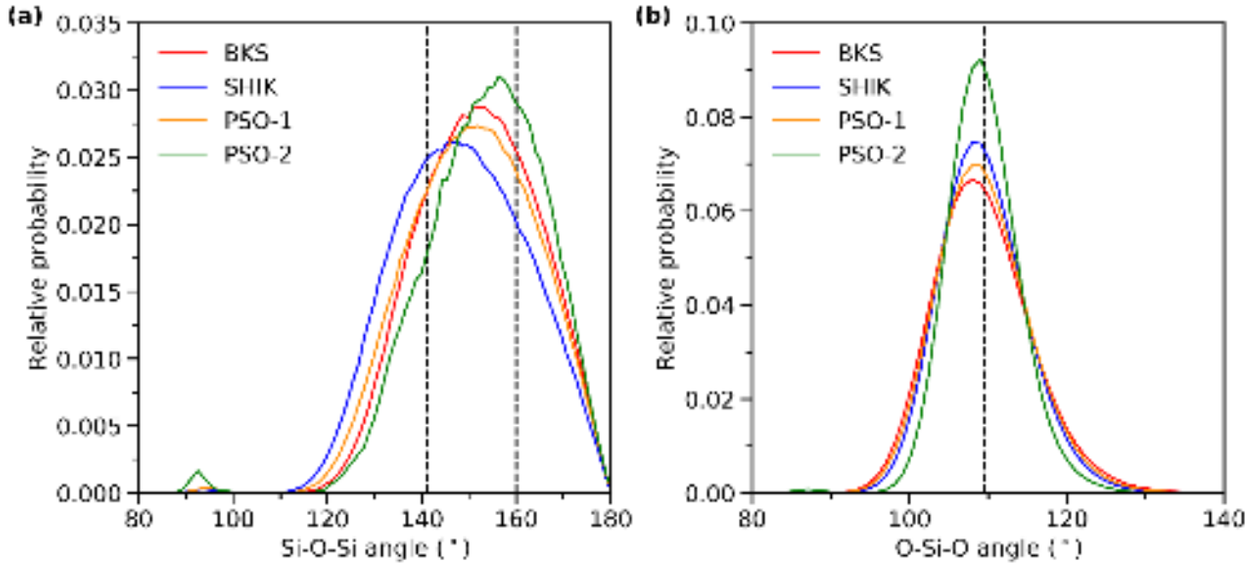

Figure 5: Partial bond angle distributions of silica glass at 300 K for (a) Si–O–Si and (b) O–Si–O. Data are shown for predictions by the PSO-1 (orange line) and PSO-2 (green line) potentials and BKS[11] (red line) and SHIK[5] (blue line) potentials from literature. The expected mean value is shown as a range between the dashed black lines from 141° to 160° for Si–O–Si[37] in (a) and as a single dashed black line at 109.5° for O–Si–O in (b).

Considering the Si–O–Si distribution (Figure 5a), we observe that the PSO-2 potential predicts an average angle of 153.4°, which is larger than that from the other potentials, though still within the range of reported experimental values[37]. For the O–Si–O PBAD (Figure 5b), we observe that all potentials predict the silica atoms to be mainly situated in tetrahedral structures with an average bond angle to oxygens of ~109°. The PSO-2 potential produces a glass structure with a narrower O–Si–O distribution compared to the other potentials, indicating that the potential yields the most ordered angular environment around the Si atom. This is in agreement with the hypothesis that the PSO-2 potential forces the simulated glass structure to be more ordered to compensate for the high cooling rate. Finally, we observe small bumps at ~90° for both PSO and SHIK potentials, which are caused by the presence of a small amount of edge-sharing SiO_4 tetrahedra. However, for all potentials except PSO-2, the amount of these unrealistic defects is negligible.

Figure 6 shows that both of the new PSO potentials describe the experimental $S(Q)$ well, with the PSO-2 potential having an $R_\chi^{S(Q)}$ of 6.1%, the lowest among all the considered potentials. This is, however, not surprising as the experimental $S(Q)$ used for comparison is the one used for obtaining the $D(r)$ function that PSO-2 is optimized to reproduce. Nonetheless, it shows that PSO-2 not only captures the short-range order of the glass structure, but also reproduces the medium-range order characterized by the $S(Q)$ function. The PSO-1 potential also predicts a reasonable $S(Q)$, giving an $R_\chi^{S(Q)}$ of 6.9%, again similar to the "soft" SHIK potential.

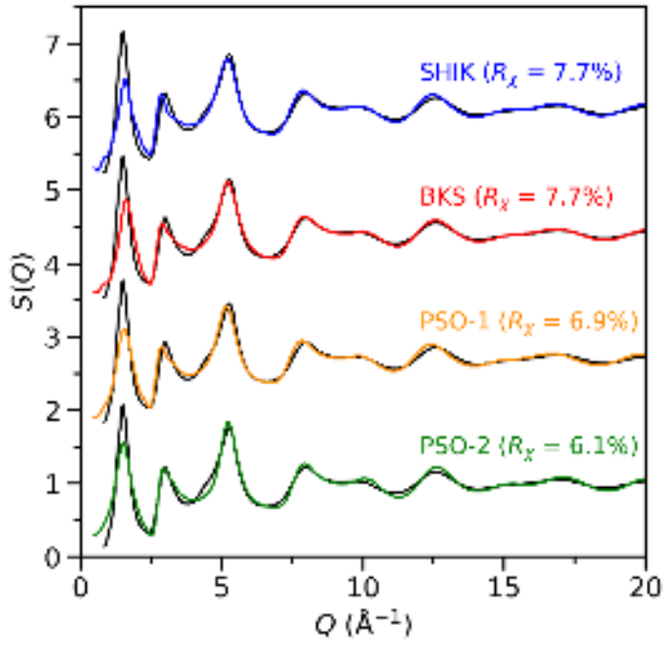

Figure 6: Neutron structure factors (*S(Q)*) for silica glass predicted by the PSO-1 (green line) and PSO-2 (orange line) potentials and BKS[11] (red line) and SHIK[5] (blue line) potentials from literature. Comparison with experimental data is also included (black line)[13] . The structure factors are displaced vertically for clarity. $R_\chi^{S(Q)}$ coefficients calculated for the structure factors are shown.

While the *S*(*Q*) does give some insight into the medium range structure, a more intuitive measure is the ring size distribution of the glass samples. These are presented in Figure 7. The ring size distribution from the four potentials do not differ significantly, although the PSO-2 potential exhibits a slightly broader distribution than the other potentials.

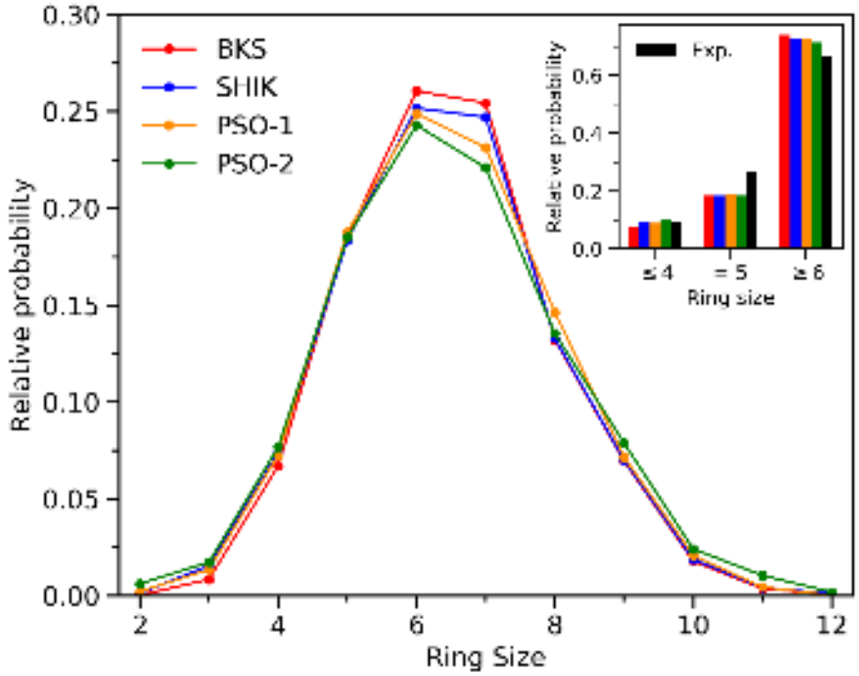

Figure 7: Ring size distribution of silica glass predicted by the PSO-1 (green line), PSO-2 (orange line), BKS[11], (red line) and SHIK[5] (blue line) potentials, compared with experimental values (black line) from literature in inset[13].

To further evaluate the performance of the PSO potentials, we have calculated the change in density, silicon coordination number, Young's modulus, and Poisson's ratio with increasing pressure (Figure 7). We observe that the PSO-1 potential correctly predicts the increase in density with pressure as seen in experiments, although with a small underprediction at lower pressures. The PSO-2 potential also shows an increase in density with increasing pressure, but the increase is much less pronounced than what is observed experimentally and for the other potentials. On the other hand, the PSO-2 potential correctly does not show any increase in silicon coordination with pressure, even at 8 GPa, whereas all the other potentials show an increase in silicon coordination. In addition, we observe a large increase in the silicon coordination number for the PSO-1 at 8 GPa compared to the increase seen for the BKS and SHIK potentials. We observe a decrease in Young's modulus for the PSO-2 potential with increasing pressure, although the overestimation previously discussed remains. For the PSO-1 potential, we observe a decrease in Young's modulus with increasing pressure until a

minimum is reached at 6 GPa. This is an overestimation of the location of the minimum when compared to the experimental data. Lastly, we observe that all potentials overestimate Poisson's ratio with no potential being able to reproduce the distinct minimum seen in experimental data. Generally, we thus conclude that the PSO potentials are not better at predicting the behavior of silica glass under pressure than the previously established potentials. This is not surprising as no information about pressure behavior was included in the cost functions used for their optimization.

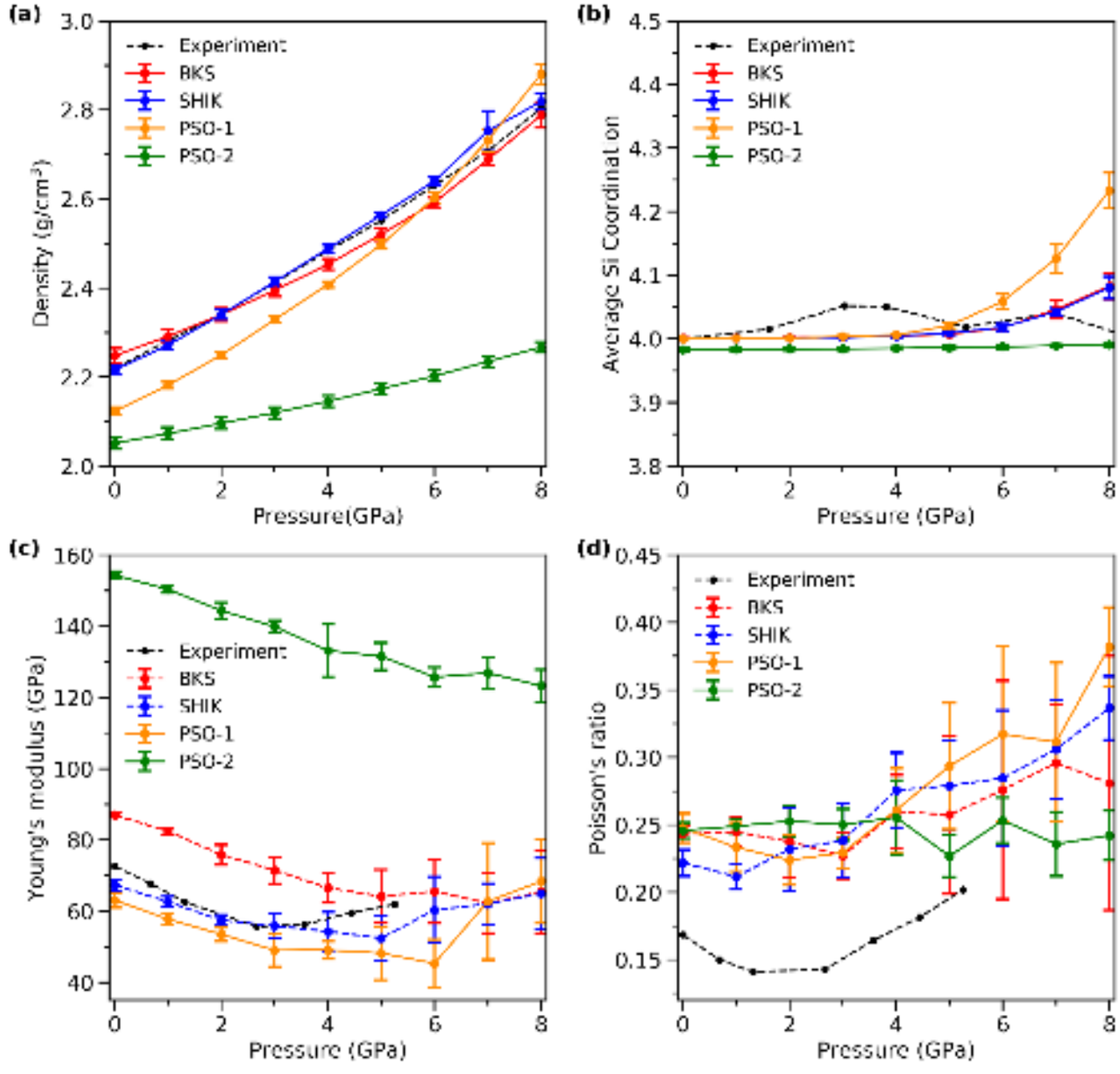

Figure 8: Variation of (a) density, (b) average Si coordination number, (c) Young's modulus, and (d) Poisson's ratio with pressure as predicted by the PSO-1 (green line), PSO-2 (orange line)

potentials, BKS[11] (red line), and SHIK[5] (blue line) potentials, along with comparison to experimental data[37–39] (dashed black line).

In theory, it is possible that a force field parameterized based on a liquid structure could offer an excellent description of the structural features of glass, assuming this glass has been prepared with a cooling rate that is comparable to experimental cooling rates. However, this is impossible to achieve with melt-quenched MD simulations, but could potentially be achieved by accelerated sampling methods like metadynamics[40] or force-enhanced atomic refinement[23].

In general, the comparison of the PSO-based with the alternative potentials from literature across different properties shows that the two new PSO potentials give a comparable description of the silica glass relative to the other potentials.

D. Optimization process

To further evaluate the performance of the PSO algorithm, we focus on the optimization process for the two potentials. Figure 9 shows the evolution in the costs obtained for all particles as a function of the iteration step number. For both optimizations, the majority of the optimization takes place in the first 70-100 iterations, where we thus observe the largest reduction in the cost of the best position found by the swarm. The last ~100 iterations primarily serve to refine the found minimum, with the best performing potential being identified after 130 and 149 iterations for PSO-1 and PSO-2, respectively. This shows that for the cost functions used herein, the PSO algorithm uses 70-100 iterations to find a very competitive minimum, corresponding to the evaluation of 1470-2100 potentials with varying parameters. We note that with the PSO parameterization, we only need to conduct the optimization once, whereas other types of conventional local optimization methods need to be repeated several times with different initial values for the parameters.

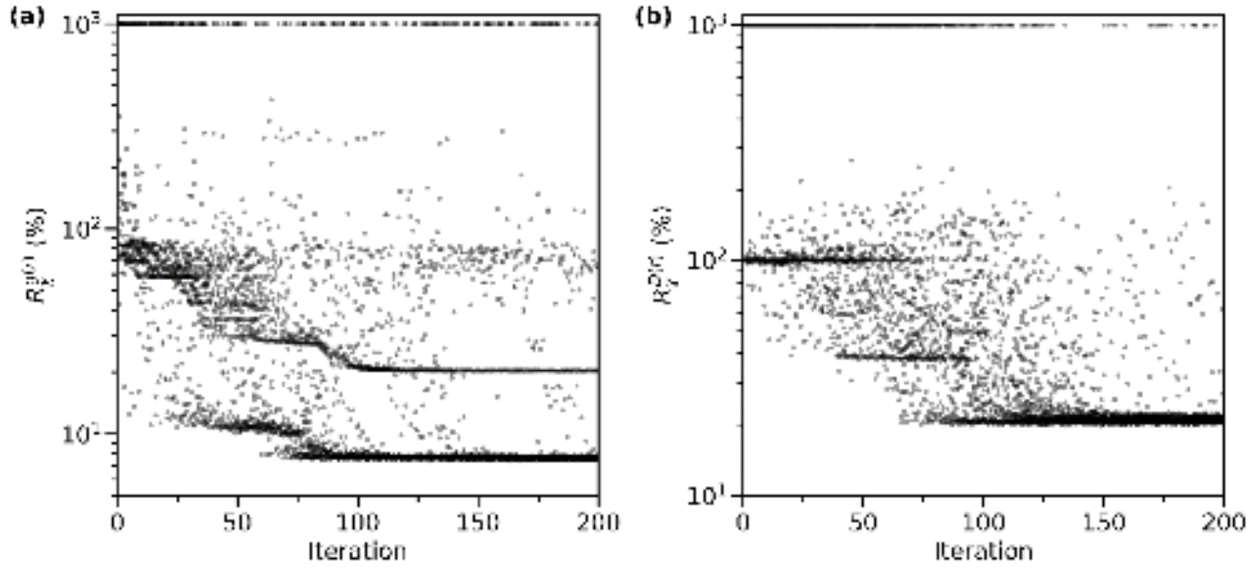

Figure 9: Development of the obtained cost for all particles as a function of iteration for (a) $R_\chi^{g(r)}$ for the PSO-1 optimization and (b) $R_\chi^{D(r)}$ for the PSO-2 optimization. Potentials, for which a cost could not be obtained, are included with a cost of 10^3.

As shown in Figure 9, there are particles with significantly higher costs than the minimum cost obtained after 200 iterations. These high costs stem from the particle swarm not being fully converged on the best-found minimum after the 200 iterations. Given more iterations, the swarm is expected to fully converge at the minimum. For the optimization of the PSO-1 potential, 242 out of the 4200 evaluated potentials could not be simulated due to the dynamics of the potential, with 184 of these being evaluated in the first 100 iterations. Similarly, for the PSO-2 optimization, 596 out of the 4200 evaluated potentials could not be simulated due to the dynamics of the potential, with 545 of these being evaluated in the first 100 iterations. These unviable potentials can be quickly dismissed and in fact provide valuable information about the cost landscape. As such, the early iterations of these PSO optimizations have been conducted significantly faster than the latter ones due to a higher occurrence of unviable potentials. The speed of the optimization process could be improved by performing the

final refinement of the best minimum found by PSO with an alternative optimization algorithm, or by changing the neighbor topology of the PSO algorithm to the global best model.

The main possible source of bias in the proposed PSO optimization scheme is the initial search space values. We choose these values based on preliminary studies, with the intent for the search space values to be large enough to contain the majority of viable parameter combinations, while limiting the amount of unviable parameter combinations. As the absorbing boundary handling scheme has only been used on the lower boundaries of the search space, particles have been able to move beyond the proposed upper search space boundary. Indeed, we observed this ability several times, with parameters of some particles reaching values more than two times higher than the upper search space boundary. We therefore do not believe that a large bias is introduced to the optimization process by providing the initial search space values.

Although the present results are for parameterization of two specific cost functions to obtain Buckingham potential parameters for silica, the approach is very general and can be easily applied to other potential parameterization schemes. However, there are still many aspects of the PSO algorithm for potential parameterization to be explored. For example, many variations of the PSO algorithm exist in literature, which could be explored to potentially increase the performance of the algorithm. The use of adaptive acceleration constants and inertia weight have been explored[41,42] and could help to achieve a better balance between exploration of the cost landscape and exploitation of known minimums. There are also variants of the PSO algorithm, in which the particles move based on other principles[43] or where it has been combined with other metaheuristic optimization methods[44]. The present application of PSO for potential parameterization can thus easily be expanded upon to achieve more efficient parameterization schemes.

IV. Conclusion

We have presented a new methodology for applying particle swarm optimization to produce accurate interatomic potentials for classical MD simulations. We demonstrate our approach by attempting to optimize the structure of SiO_2 in both the molten and glassy states using the Buckingham potential form. Generally, we find the particle swarm algorithm to be highly efficient at searching for and identifying viable potential parameters, which reproduce the structural features used in the parameterization. Although the results presented here are for parameterization of two specific cost functions to obtain Buckingham potential parameters for silica, the approach is very general and can be easily applied to other potential parameterization schemes. As such, our work has shown that it is possible using particle swarm optimization to minimize rough cost functions with an efficient and non-biased approach. The PSO method therefore provides a suitable algorithm for parametrizing new interatomic potentials.

Supplementary material

See the supplementary material for figures showing the atomic pair interactions and predicted VDOS of silica glass of the PSO potentials compared to potentials from literature.

Data availability

The data supporting the results within this paper are available from the corresponding authors upon reasonable request.

Acknowledgements

We thank Aalborg University for access to computational resources through CLAAUDIA. M.B. acknowledges funding from the National Science Foundation under Grants Nos. DMR-1928538 and DMR-1944510.

Competing interests

The authors declare no competing interests.

References

[1] J.D. Musgraves, J. Hu, and L. Calvez, *Springer Handbook of Glass* (Springer, 2019).

[2] J.C. Mauro, Curr. Opin. Solid State Mater. Sci. **22**, 58 (2018).

[3] M. Bauchy, Comput. Mater. Sci. **159**, 95 (2019).

[4] L. Huang and J. Kieffer, in *Mol. Dyn. Simulations Disord. Mater. From Netw. Glas. to Phase-Change Mem. Alloy.*, edited by C. Massobrio, J. Du, M. Bernasconi, and P.S. Salmon (Springer International Publishing, Charm, 2015), pp. 87–112.

[5] S. Sundararaman, L. Huang, S. Ispas, and W. Kob, J. Chem. Phys. **148**, (2018).

[6] A. Carré, S. Ispas, J. Horbach, and W. Kob, Comput. Mater. Sci. **124**, 323 (2016).

[7] H. Liu, Z. Fu, Y. Li, N.F.A. Sabri, and M. Bauchy, MRS Commun. **9**, 593 (2019).

[8] D. Wang, D. Tan, and L. Liu, Soft Comput. **22**, 387 (2018).

[9] D. González and S. Davis, Comput. Phys. Commun. **185**, 3090 (2014).

[10] Z. Liu, Q. Han, Y. Guo, J. Lang, D. Shi, Y. Zhang, Q. Huang, H. Deng, F. Gao, B. Sun, and S. Du, J. Alloys Compd. **780**, 881 (2019).

[11] B.W.H. van Beest and G.J. Kramer, Phys. Rev. Lett. **64**, 1955 (1990).

[12] B. Guillot and N. Sator, Geochim. Cosmochim. Acta **71**, 1249 (2007).

[13] Y. Shi, D. Ma, A.P. Song, B. Wheaton, M. Bauchy, and S.R. Elliott, J. Non. Cryst. Solids **528**, 119760 (2020).

[14] S. Plimpton, J. Comput. Phys. **117**, 1 (1997).

[15] C.J. Fennell and J.D. Gezelter, J. Chem. Phys. **124**, (2006).

[16] A. Carré, L. Berthier, J. Horbach, S. Ispas, and W. Kob, J. Chem. Phys. **127**, (2007).

[17] Z. Zhang, S. Ispas, and W. Kob, J. Non. Cryst. Solids **532**, 119895 (2020).

[18] A.N. Cormack, J. Du, and T.R. Zeitler, Phys. Chem. Chem. Phys. **4**, 3193 (2002).

[19] H. Liu, Z. Fu, Y. Li, N.F.A. Sabri, and M. Bauchy, J. Non. Cryst. Solids **515**, 133 (2019).

[20] D.A. Keen, J. Appl. Crystallogr. **34**, 172 (2001).

[21] V.F. Sears, Neutron News **3**, 26 (1992).

[22] S.S. Sørensen, H. Johra, J.C. Mauro, M. Bauchy, and M.M. Smedskjaer, Phys. Rev. Mater. **3**, (2019).

[23] Q. Zhou, T. Du, L. Guo, M.M. Smedskjaer, and M. Bauchy, J. Non. Cryst. Solids **536**, 120006 (2020).

[24] Y. Shi, N.T. Lonnroth, R.E. Youngman, S.J. Rzoska, M. Bockowski, and M.M. Smedskjaer, J. Non. Cryst. Solids **483**, 50 (2018).

[25] J.I. Gersten, *The Physics and Chemistry of Materials.* (Wiley New York, New York, 2001).

[26] S. Le Roux and P. Jund, Comput. Mater. Sci. **49**, 70 (2010).

[27] F. Van Den Bergh and A.P. Engelbrecht, Inf. Sci. (Ny). **176**, 937 (2006).

[28] E.G. Talbi, *Metaheuristics: From Design to Implementation* (Wiley, 2009).

[29] D. Bratton and J. Kennedy, Proc. 2007 IEEE Swarm Intell. Symp. SIS 2007 120 (2007).

[30] S. Kiranyaz, T. Ince, and M. Gabbouj, in *Adapt. Learn. Optim.* (2014), pp. 45–82.

[31] J. Kennedy, in *Handb. Nature-Inspired Innov. Comput. Integr. Class. Model. with Emerg. Technol.*, edited by A. Zomaya (Springer, 2006).

[32] M. Clerc and J. Kennedy, IEEE Trans. Evol. Comput. **6**, 58 (2002).

[33] J. Robinson and Y. Rahmat-Samii, IEEE Trans. Antennas Propag. **52**, 397 (2004).

[34] H. Liu, Y. Li, Z. Fu, K. Li, and M. Bauchy, J. Chem. Phys. **152**, (2020).

[35] W. Pabst and E. Gregorová, Ceram. - Silikaty **57**, 167 (2013).

[36] Z. Liu, Y. Hu, X. Li, W. Song, S. Goyal, M. Micoulaut, and M. Bauchy, Phys. Rev. B **98**, 1 (2018).

[37] A. Zeidler, K. Wezka, R.F. Rowlands, D.A.J. Whittaker, P.S. Salmon, A. Polidori, J.W.E. Drewitt, S. Klotz, H.E. Fischer, M.C. Wilding, C.L. Bull, M.G. Tucker, and M. Wilson, Phys. Rev. Lett. **113**, 1 (2014).

[38] O.B. Tsiok, V. V. Brazhkin, A.G. Lyapin, and L.G. Khvostantsev, Phys. Rev. Lett. **80**, 999 (1998).

[39] A. Yokoyama, M. Matsui, Y. Higo, Y. Kono, T. Irifune, and K.I. Funakoshi, J. Appl. Phys. **107**, (2010).

[40] I. Ronneberger and R. Mazzarello, in *Mol. Dyn. Simulations Disord. Mater. From Netw. Glas. to Phase-Change Mem. Alloy.*, edited by C. Massobrio, J. Du, M. Bernasconi, and P.S. Salmon (Springer International Publishing, Charm, 2015), pp. 57–85.

[41] K.R. Harrison, A.P. Engelbrecht, and B.M. Ombuki-Berman, Swarm Intell. **10**, 267 (2016).

[42] K.R. Harrison, A.P. Engelbrecht, and B.M. Ombuki-Berman, Swarm Intell. **12**, 187 (2018).

[43] S. Cheng, H. Lu, X. Lei, and Y. Shi, Complex Intell. Syst. **4**, 227 (2018).

[44] S. Sengupta, S. Basak, and R. Peters, Mach. Learn. Knowl. Extr. **1**, 157 (2018).

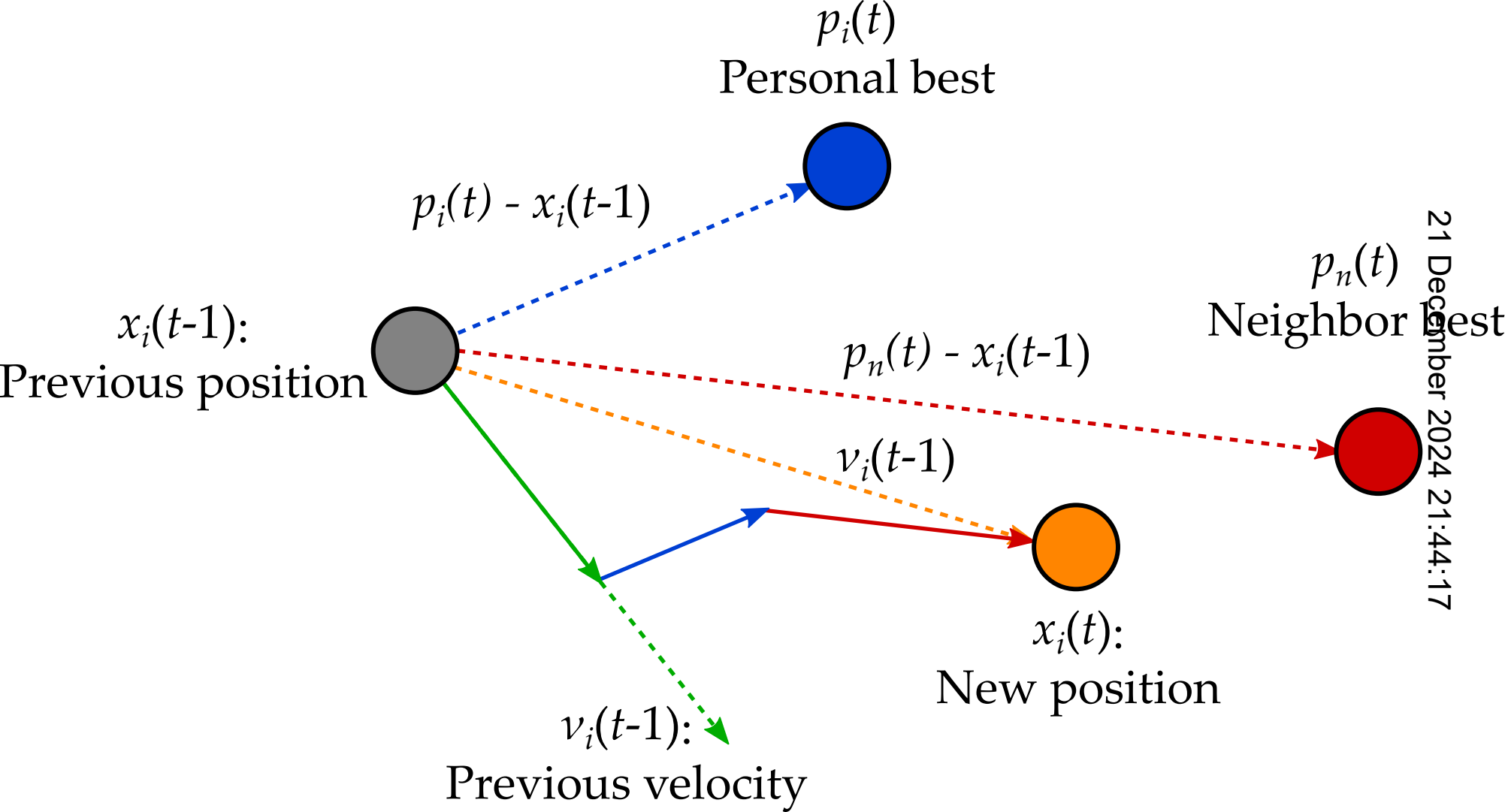

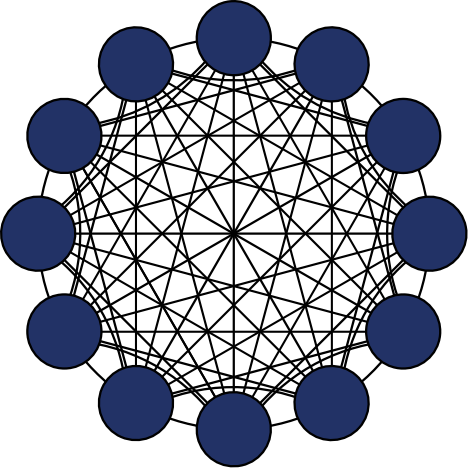

(a) global best topology

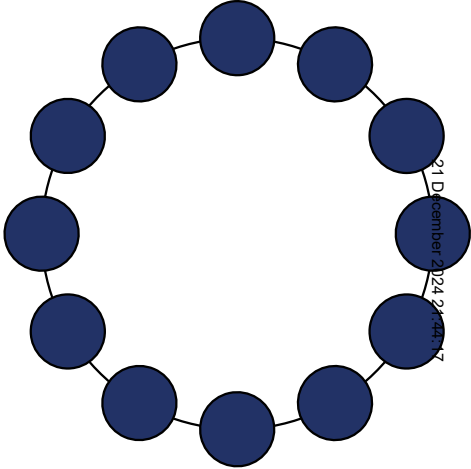

(b) local best topology

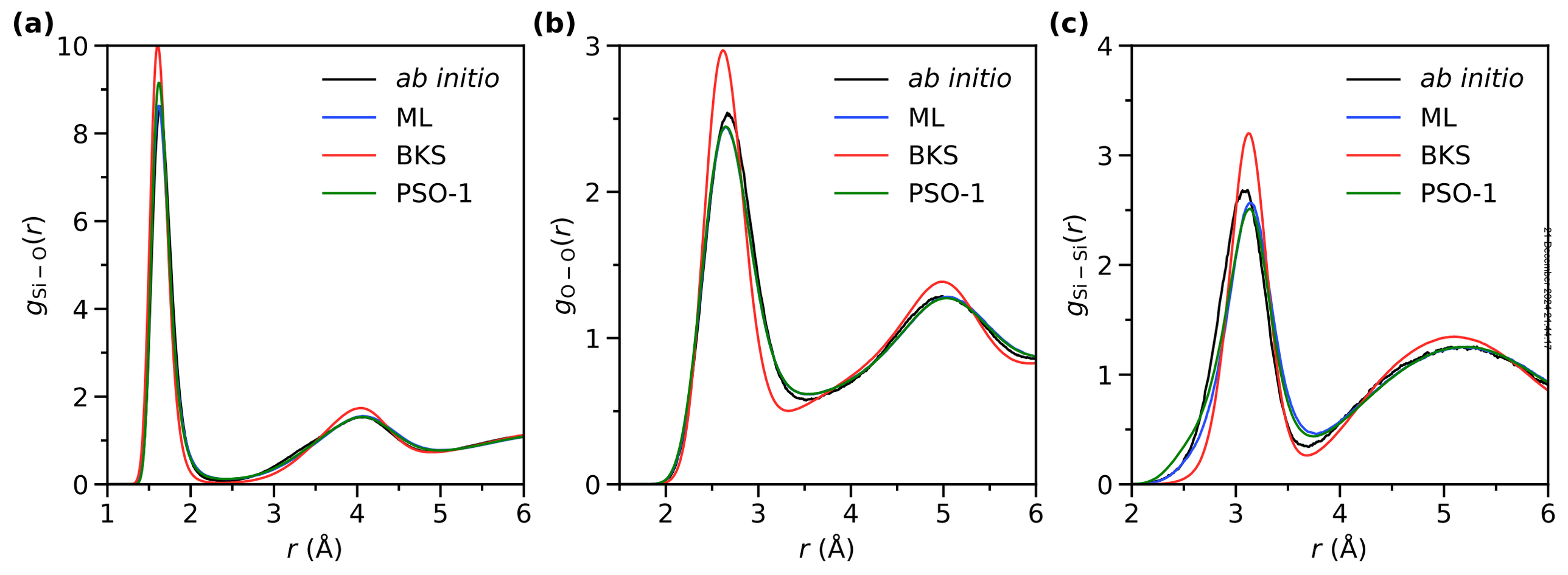
(a)
(b)
(c)
ab initio
ML
BKS
PSO-1
$g_{Si-O}(r)$
$g_{O-O}(r)$
$g_{Si-Si}(r)$
r (Å)
21 December 2024 21:11:17

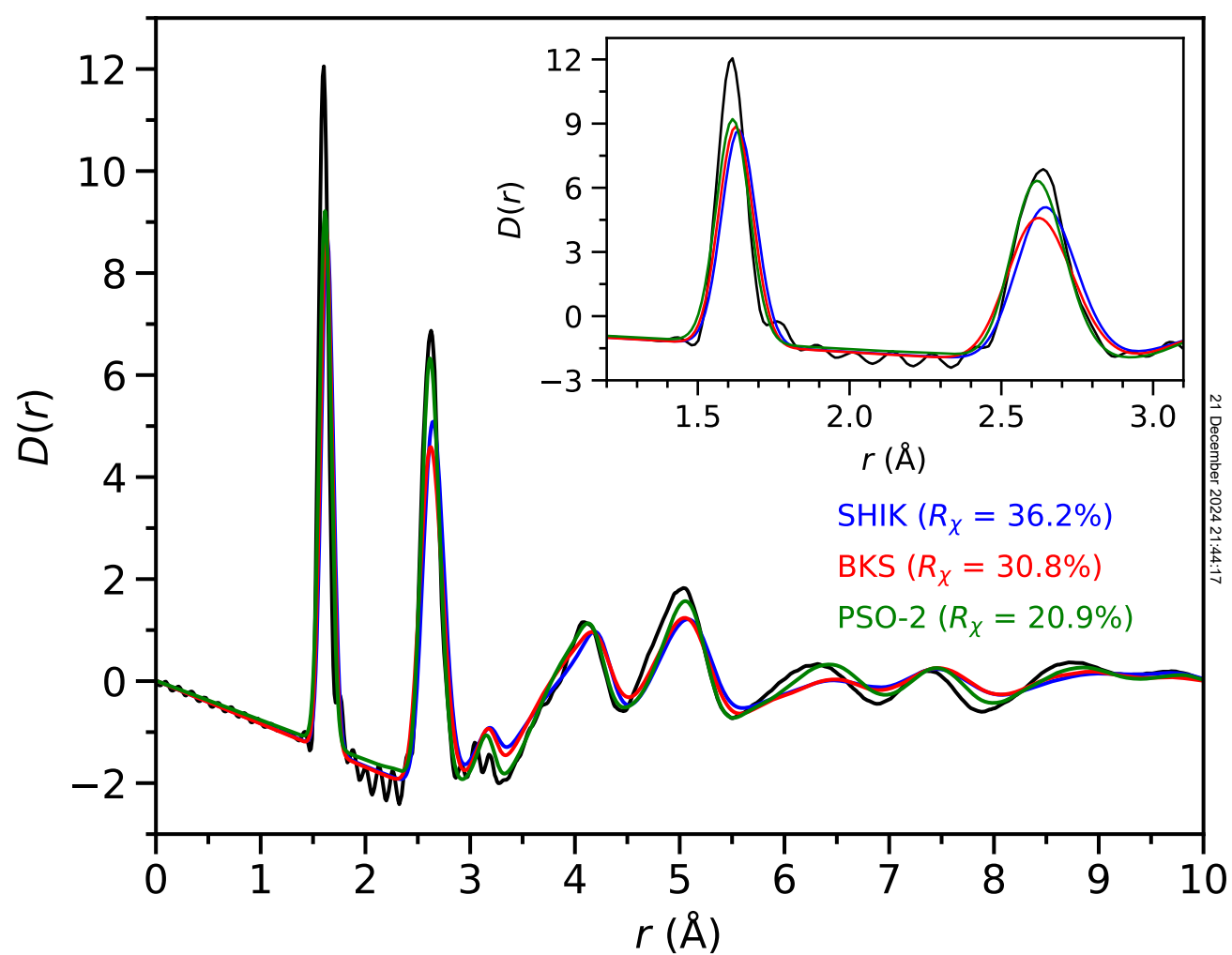
D(r)
r (Å)
SHIK (R_χ = 36.2%)
BKS (R_χ = 30.8%)
PSO-2 (R_χ = 20.9%)
21 December 2024 21:44:17

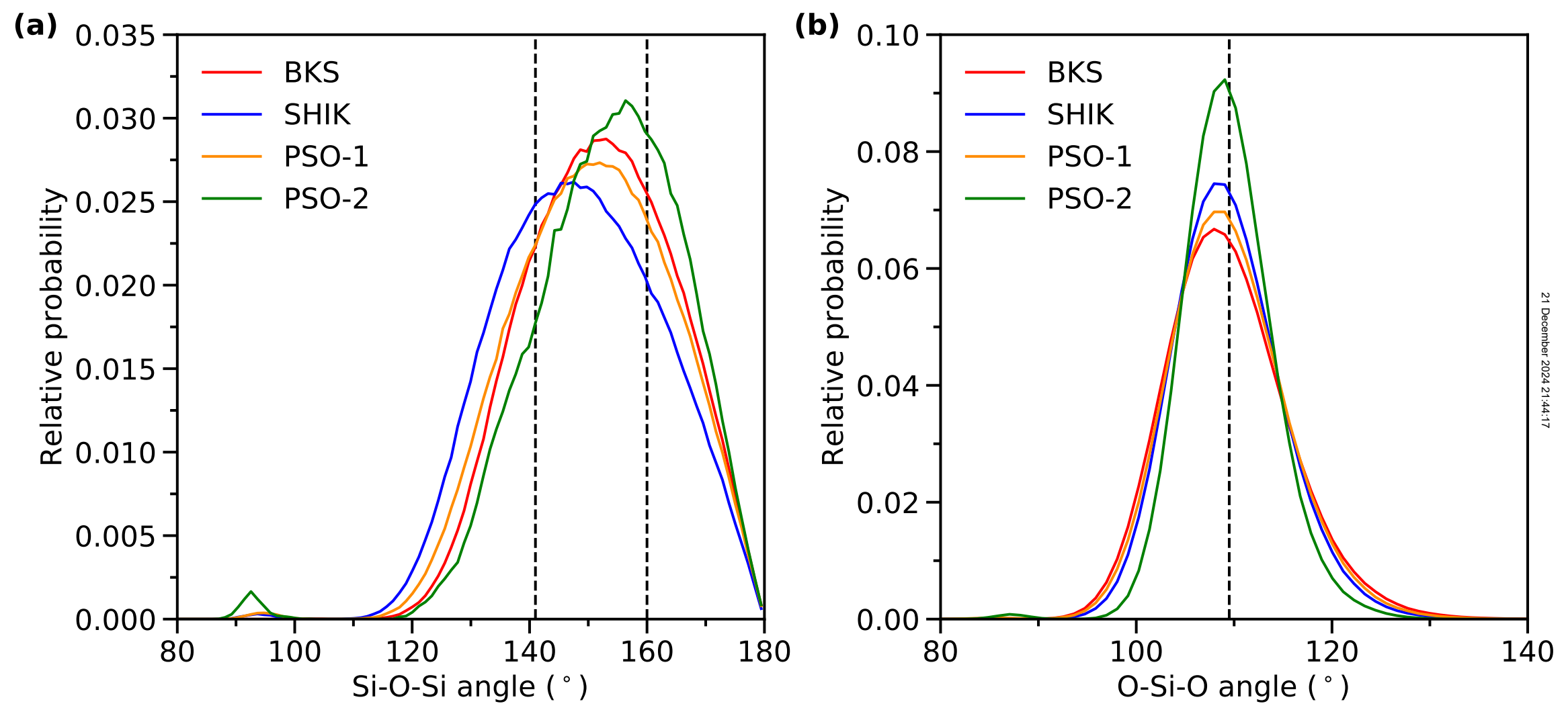
(a)
(b)
BKS
SHIK
PSO-1
PSO-2
Relative probability
Si-O-Si angle (°)
O-Si-O angle (°)
0.035
0.030
0.025
0.020
0.015
0.010
0.005
0.000
0.10
0.08
0.06
0.04
0.02
0.00
80
100
120
140
160
180
21 December 2024 21:44:17

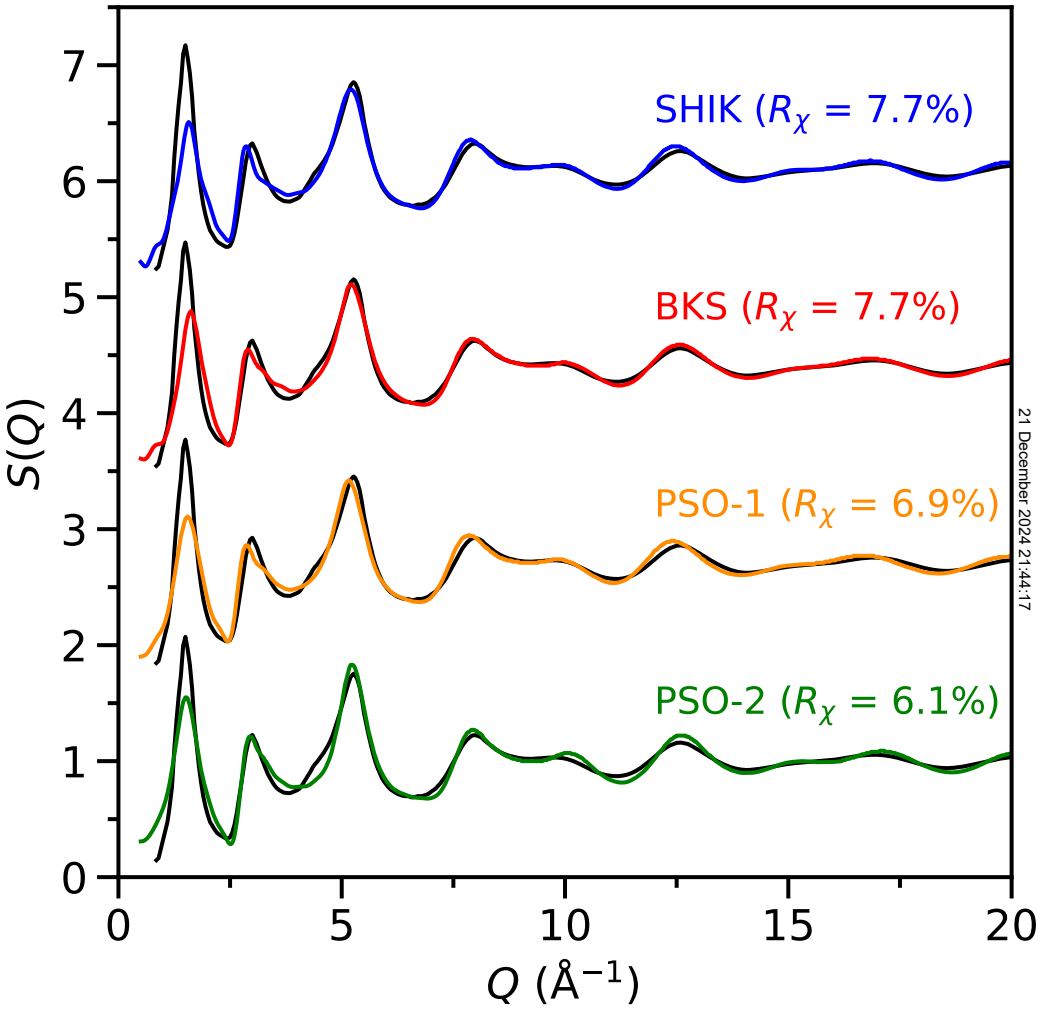
SHIK (R_χ = 7.7%)
BKS (R_χ = 7.7%)
PSO-1 (R_χ = 6.9%)
PSO-2 (R_χ = 6.1%)
$S(Q)$
Q (Å^{-1})
0
1
2
3
4
5
6
7
0
5
10
15
20
21 December 2024 21:44:17

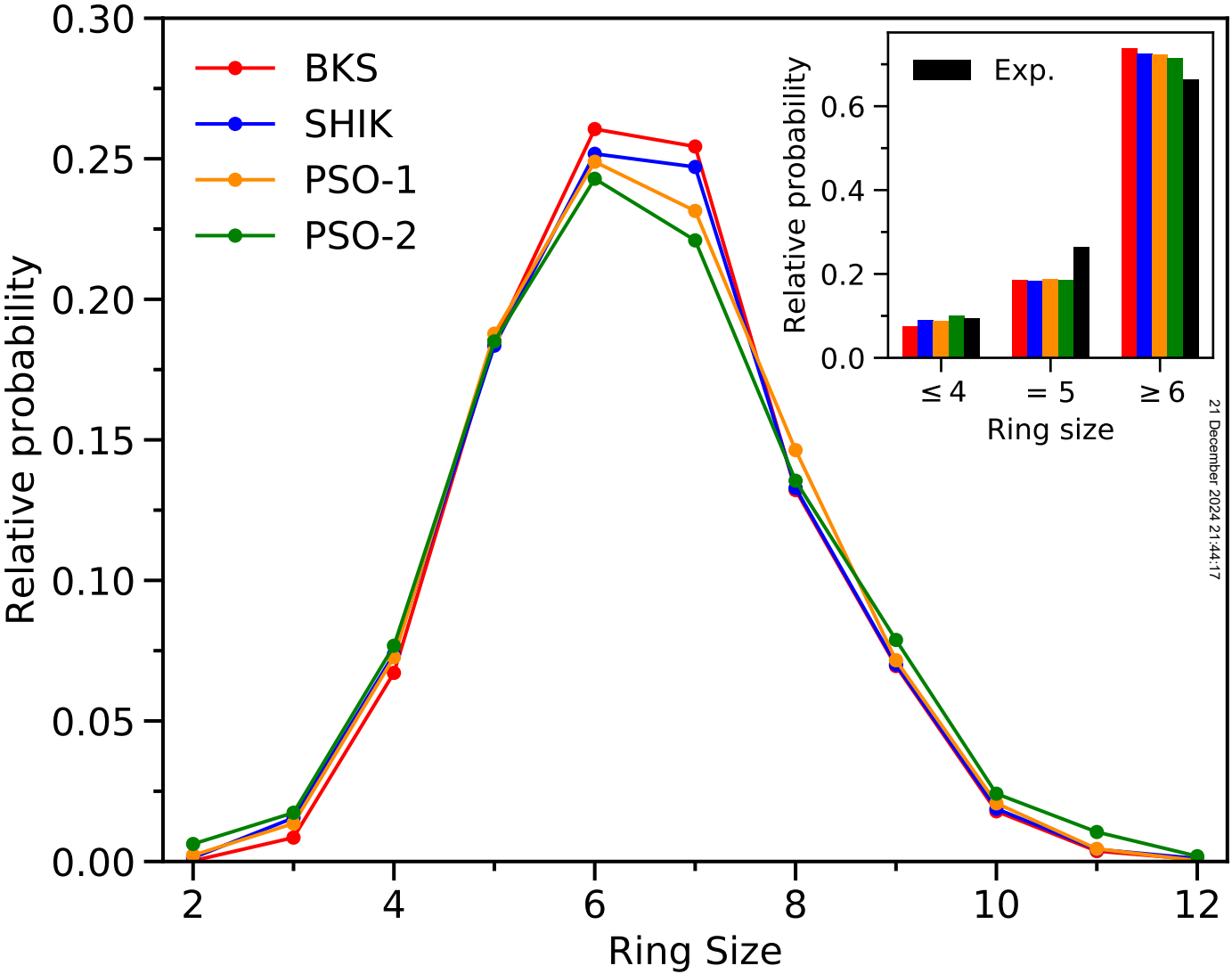
BKS
SHIK
PSO-1
PSO-2
Relative probability
Ring Size
0.00
0.05
0.10
0.15
0.20
0.25
0.30
2
4
6
8
10
12
Exp.
Relative probability
0.0
0.2
0.4
0.6
≤ 4
= 5
≥ 6
Ring size
21 December 2024 21:44:17

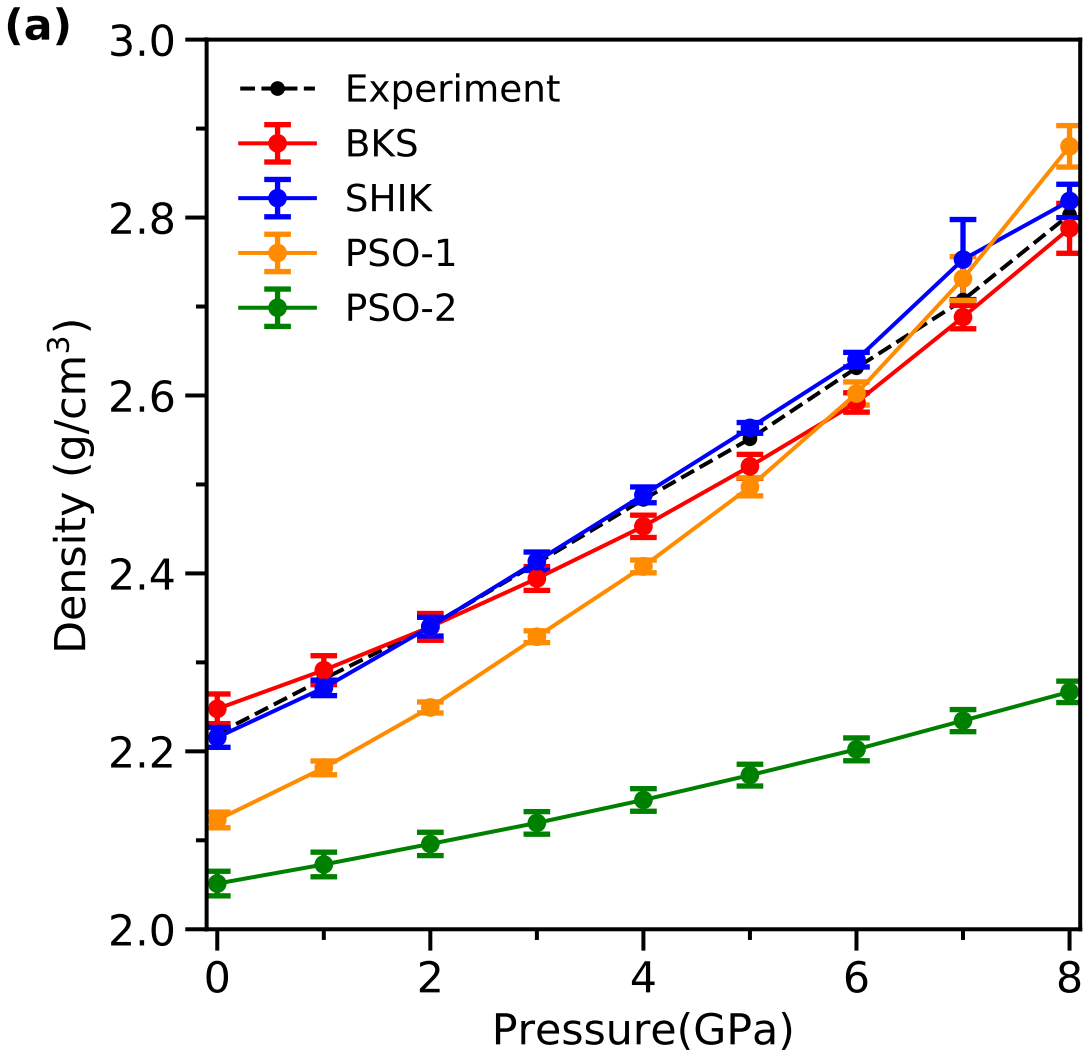
(a)
Experiment
BKS
SHIK
PSO-1
PSO-2
Density (g/cm^3)
Pressure(GPa)

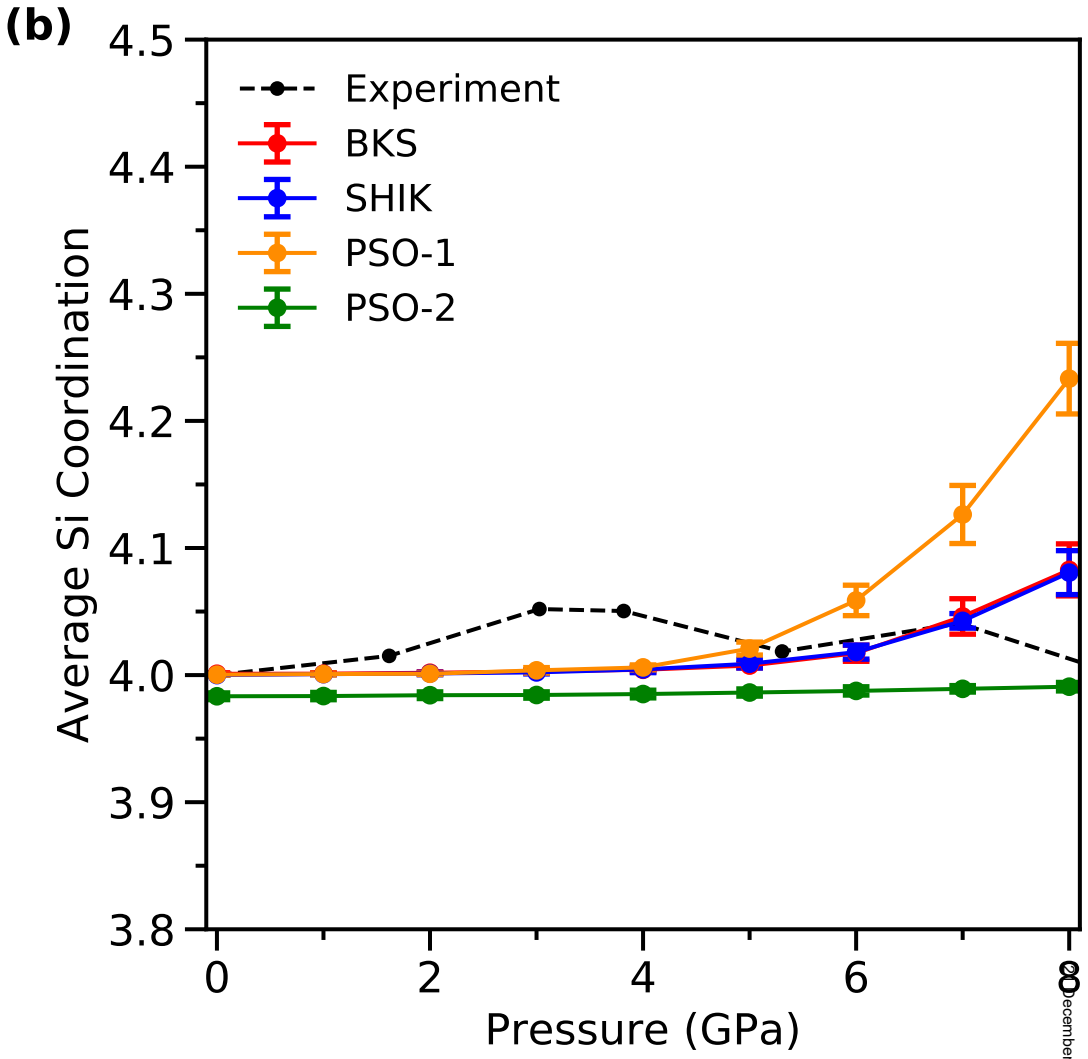
(b)
Experiment
BKS
SHIK
PSO-1
PSO-2
Average Si Coordination
Pressure (GPa)

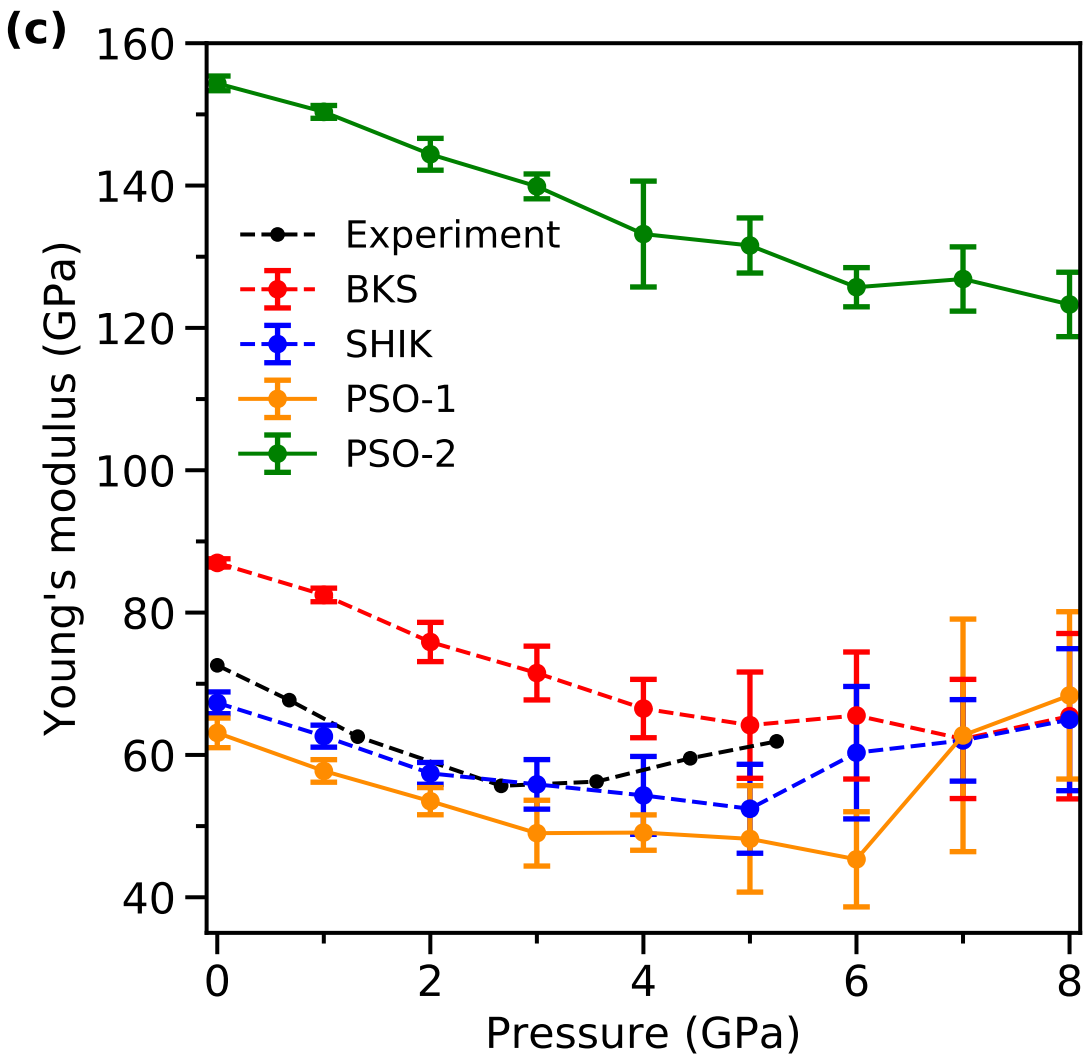
(c)
Experiment
BKS
SHIK
PSO-1
PSO-2
Young's modulus (GPa)
Pressure (GPa)

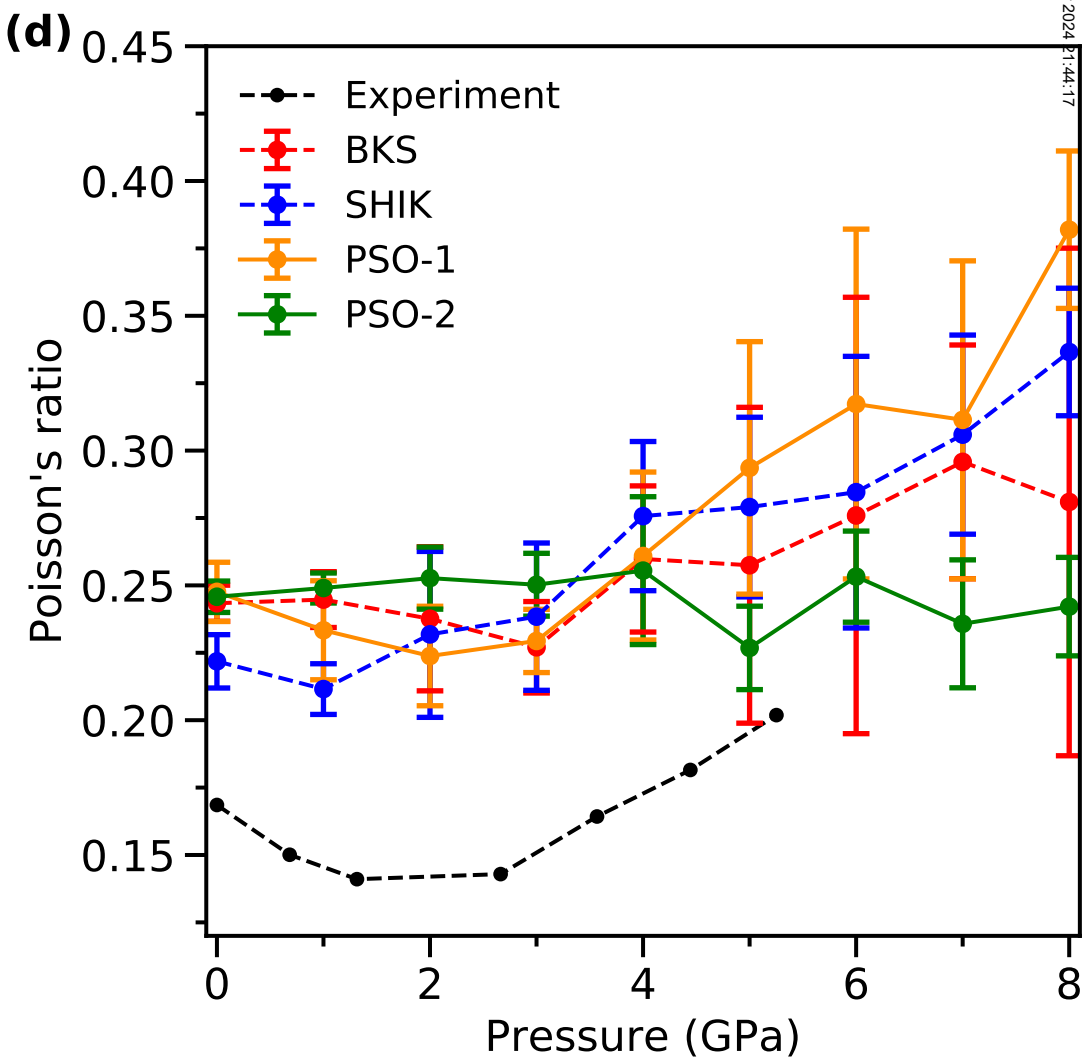
(d)
Experiment
BKS
SHIK
PSO-1
PSO-2
Poisson's ratio
Pressure (GPa)

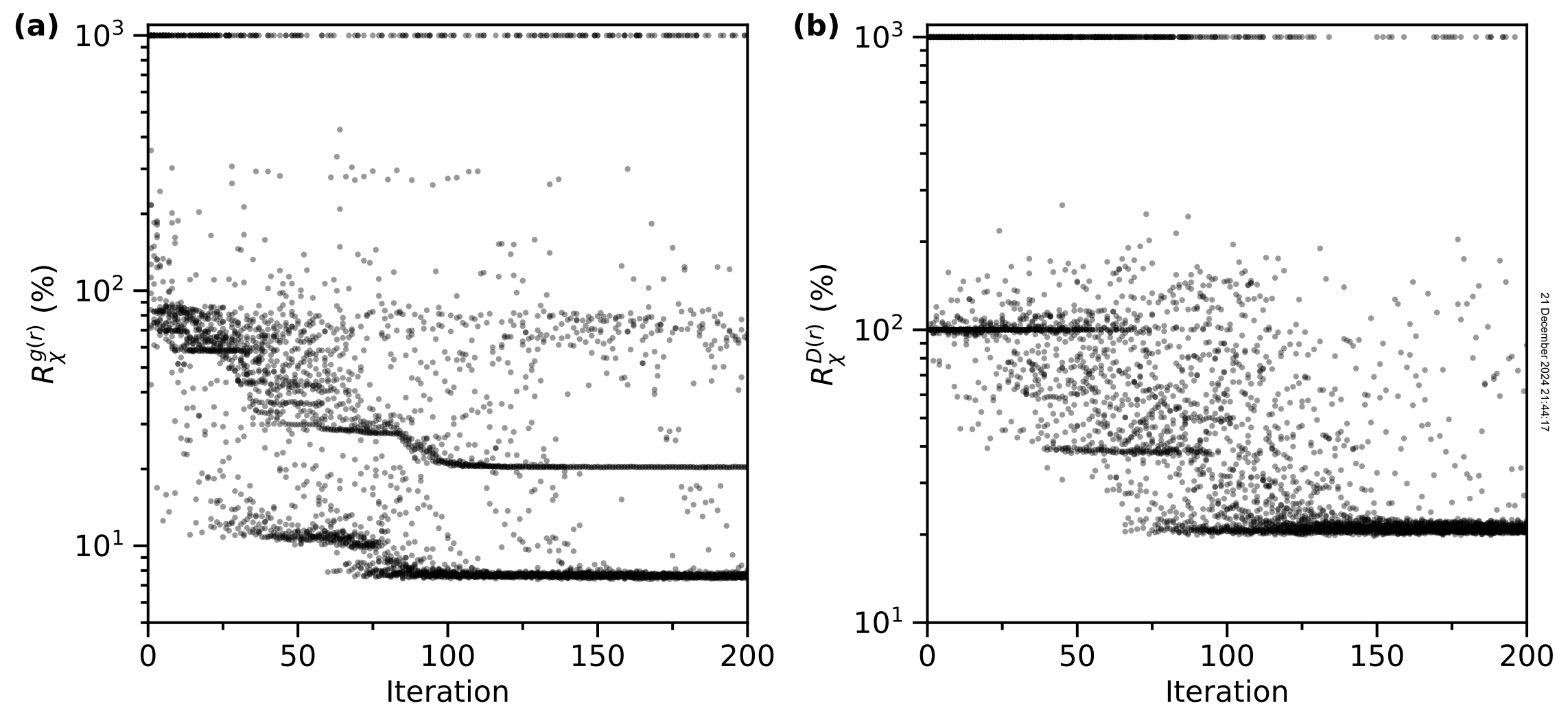
(a)
(b)
10^3
10^2
10^1
$R_\chi^{g(r)}$ (%)
$R_\chi^{D(r)}$ (%)
0
50
100
150
200
Iteration
21 December 2024 21:44:17